ABSTRACT

HACKNEY, DREW ALEXANDER. Embedded Fiber Bragg sensors for Damage Identification in Sandwich Composites After Impact. (Under the direction of Kara J. Peters.)

This study investigates the use of fiber Bragg gratings (FBGs) for damage identification in sandwich composite structures subjected to multiple low velocity impact events. Initially, a set of twelve graphite-fiber-epoxy facesheet / Rohacell foam core sandwich composite specimens were tested to characterize their impact response. Each test consisted of repeated low-velocity impacts at a constant impact energy to measure the contact force and dissipated energy per strike and observe damage progression throughout the composite lifetime. The maximum contact force decreased slightly while the dissipated energy increased over the lifetime of the composite. Infrared thermography images were also taken of a specimen to provide comparison with a conventional non-destructive evaluation method for the detection of damage in sandwich composites. The infrared thermography detected damage to the impacted facesheet which was visible on the surface and highlighted shear cracking in the foam core (when imaged from the specimen side). The infrared thermography was not able to detect the extensive core crushing or facesheet-core interface damage present at the end of the laminate lifetime. Similar low-velocity impact testing was performed on sandwich composites with a single optical fiber embedded in the adhesive bond between the core and the faceplate. The presence of the optical fiber did reduce the average specimen lifetime but not the specimen stiffness.

The final set of specimens included a FBG sensor in the embedded optical fiber. The peak wavelength of the FBG sensor was interrogated at 1 kHz throughout each impact event, while the full-spectral response of the FBG sensor was measured in between impact events. From the peak wavelength shift measurements, the interfacial residual strain was calculated. For all specimens this residual strain initially increased with strike number and then decreased. In some specimens, a final region of increasing residual strain was observed. These observations were combined with an analysis of the shape of the reflected spectrum and photographs of the sandwich composite surface to further understand the state of damage. The FBG response spectra were distorted due to transverse loading on the optical fiber present after fracture of the impacted facesheet, typically after crushing of the core in the vicinity of the impact. The form of the reflected spectra can thus be used as an in-situ indicator of the presence of core-crushing and potential core-facesheet debonding

Embedded Fiber Bragg Sensors for Damage Identification in
Sandwich Composites After Impact

by
Drew Alexander Hackney

A thesis submitted to the Graduate Faculty of
North Carolina State University
in partial fulfillment of the
requirements for the Degree of
Master of Science

Mechanical Engineering

Raleigh, North Carolina

2010

APPROVED BY:

Dr. Mohammed Zikry

Dr. Jeff Eischen

Dr. Kara Peters
Chair of Advisory Committee

BIOGRAPHY

Drew Hackney was born in Rockville, MD on April 1st, 1986 to Stephen and Paige Hackney before moving to Houghton, MI before his first birthday. Drew has two brothers, Eric who is one year older, and Brian who is three years younger. Drew attended Houghton Elementary School, Houghton Middle School, and Houghton High School where he played soccer. Drew graduated from Houghton High School in 2004 as a recipient of the Michigan Achievement Award.

Drew attended Cedarville University in Cedarville, OH where he was the recipient of the President's Scholarship and where he majored in Mechanical Engineering. While at Cedarville, Drew participated in intramural soccer, softball, and the university pep band. He also worked with Children's Medical Center of Dayton to help develop and assistive gait trainer for children with mild motor disabilities to learn proper gait techniques. His work on this project earned him an award from the annual student design competition held by the Rehabilitation Engineering and Assistive Technology Society of North America (RESNA).

Upon completion of his undergraduate degree, Drew continued his education by pursuing his Master's degree in Mechanical Engineering at North Carolina State University. While at North Carolina State University, Drew has been active in Vintage 21 Church. He has also joined the Optical Sensing and Monitoring Laboratory under the supervision of Dr. Kara Peters. His research pertains to the study of embedded fiber Bragg grating sensors in sandwich composites consisting of carbon fiber reinforce polymer (CFRP) facesheets and foam cores.

ACKNOWLEDGEMENTS

Drew would like to thankfulness to his advisor, Dr. Kara Peters for her patience during this project as well as for her invaluable guidance and expertise. Drew also thanks the members of his thesis committee, Drs. Mohammed Zikry and Jeff Eischen.

Drew would like to acknowledge the partial support of the National Science Foundation through grant number CMMI 0825709.

Drew would personally like to thank Skip Richardson and Mike Breedlove from the Department of Mechanical and Aerospace Engineering's machine shop for their manufacturing assistance. Sachin Pawar for his assistance with setting up and explaining the thermography, and Lindsey Barr for her valuable assistance of the summer.

Finally, Drew would like to express his gratitude to his family, specifically his parents for their continual support and encouragement throughout this project.

TABLE OF CONTENTS **PAGE**

LIST OF TABLES **PAGE**

LIST OF FIGURES **PAGE**

PAGE

PAGE

CHAPTER 1. INTRODUCTION

Overview

The goal of this study is to investigate the information gained from fiber Bragg gratings for damage identification in sandwich composite structures subjected to multiple low velocity impact events. First, the macromechanical behavior of woven carbon-fiber-epoxy, foam core sandwich composites under low velocity impact testing was experimentally measured. Infrared thermography images were also taken of a specimen throughout its lifetime to provide a comparison between the identification from the embedded sensors and a conventional non-destructive evaluation method. Next, an optical fiber was embedded in several specimens to determine how the presence of a fiber affected the behavior of the composite and evaluate the survivability of the optical fiber within the structure. Finally specimens with embedded fiber Bragg grating (FBG) sensors were subjected to multiple low-velocity impacts until failure. A tunable filter laser system was used to interrogate the embedded sensor during and after each impact to measure damage. The shift in peak wavelength was determined during each strike, while a full spectral sweep was completed between strikes to measure the distortion of the spectrum caused by the impact. From these results, the feasibility of FBG sensors for structural health monitoring of foam core sandwich composites is demonstrated.

Chapter 1 provides the goals of this study and presents a literature review of the low-velocity impact response of sandwich composites, as well as previous attempts to monitor their response through embedded sensors. Chapter 2 details the specimen fabrication techniques used and the experimental testing procedures. Chapter 3 presents the experimental results of the impact testing, infrared thermography imaging and FBG sensor interrogation. Changes in the peak wavelength shifts, residual average strains and full spectral response of the FBG sensor are correlated to the dominant failure modes in the progression of damage in the sandwich composite. Finally, Chapter 4 presents the conclusions of the study and proposes future work for this research area.

Low-velocity impact damage in sandwich composites

Sandwich composites are being rapidly integrated into aerospace and marine structures due to their lightweight, high rigidity characteristics. This elevated rigidity comes through stiff facesheets, which carry the principal loads, separated by a lightweight core that transmits loads between them through shear (Nemes and Simmonds, 1992). Ideally, the core consists of a material that is both high strength and complaint (Caprino and Teti, 1994). Common core materials are cellular foams, balsa wood, trusses, and metallic and non-metallic honeycombs (Daniel and Ishai, 2006). The work of this thesis will focus on foam core sandwich composites.

The juxtaposition of the highly deformable core with the inflexible facesheets weakens the sandwich composites resistance to impact damage. As impact events are often encountered in aerospace and marine applications, designing sandwich composites that are damage tolerant is of extreme importance. Empirical, experimental studies have been primarily applied to predicting the strength after impact of sandwich composites as comprehensive analytical models are not available (Caprino and Teti, 1994). Additionally, scaling these models to predict the impact performance of full-scale components can present difficulties. The residual strength of a sandwich composite is directly related to the size and depth of the impact damage and can be significantly smaller than the strength of the pristine composite, without large indications on the surface (Avrashi *et al.*, 1995; Schubel *et al.*, 1997; Lee *et al.*, 1993).

The damage in sandwich composites subjected to low velocity impacts can be broken up into three distinct classifications: facesheet damage, facesheet-core interface damage, and core damage, as shown in Fig. 1.1. Damage to the impacted facesheet is through matrix cracking and delamination, with fiber breakage occurring at higher impact energies (Caprino and Teti, 1994). Significant indentation of the facesheet can often occur at the impact location as a result of the fiber breakage. The exact order and relative size of these failure modes depends upon the facesheet configuration.

The damage in the core of foam core sandwich composite structures can be classified as either core cracking or core crushing. As a result of impact loading, a shear crack appears in the core originating at the impact site on the top facesheet, and propagates through the core to the lower facesheet. This crack is due to shear failure of the foam and therefore inclined at 40-45 degrees, starting at the surface away from the impacted facesheet. The crack propagates through the foam core and then branches into facesheet-core delaminations (Wu and Sun, 1996). While the delamination is the dominate failure mode, the shear bands themselves have minimal effect on the residual strength and are highly dependent on the specimen size and boundary conditions (Anderson and Madenci, 2000).

Extensive core crushing is often present well before significant damage to the face sheet is present (Anderson and Madenci, 2000; Lee *et al.*, 1993). However, this core damage does not typically have a strong influence on the post-impact residual strength of the sandwich composite as a complete structure (Leijten *et al.*, 2009). Core crushing is caused by the collapse of foam cells due to cell wall buckling or breakage, creating a cavity within the core. The cavity typically has a larger area than the impact site and is invisible to surface inspection (Caprino and Teti, 1994). Akil Hazizan and Cantwell (2002), Shipsha *et al.* (2003), Torre and Kenny (2000), and Lee *et al.* (1998) have shown that the cavity in the foam greatly diminishes performance of the structure. Core crushing is the dominant critical mode of failure sandwich composite structures. As such, strengthening the core with nanoclays and pins have been applied to protect against core crushing (Vaidya *et al.*, 2001; Hoshur *et al.*, 2008). While effective, both these methods significantly increase the weight of the structure.

Delamination at the skin-core interface often plays a critical role towards the loss of structural integrity in the form of reduced bending stiffness and strength (Nemes and Simmonds, 1992). Facesheet-core delamination is typically induced by intra-matrix cracking in the foam core on each side of the impact. Combined with facesheet cracking, facesheet-core debonding can also permit moisture ingression into the sandwich core, further degrading the integrity of the facesheet to core bond and the core material itself. To further complicate matters, facesheet cracking can sometimes appear prior to interface delamination, increasing the rate of the moisture induced degradation (Bernard and Lagace, 1989).

Finally, even at elevated impact energies, damage is typically not present in the facesheet opposite to the impacted surface due to the high deformability of the core which localizes the damage zone around the impact location (Caprino and Teti, 1994).

For an equal impact energy, sandwich composite structures with denser cores and thicker faceplates are more resistant to damage than those with thinner faceplates and lower-density cores (Anderson and Madenci, 2000). However, a high density core does not necessarily protect against localized fiber breakage in the facesheets. Caprino and Teti (1994), Akil Hazizan and Cantwell (2002), and Freeman *et al.* (2005) showed that though a higher density core does better support the facesheets against deflection, it can also increase the contact force for a given impact energy. There is therefore a need to better understand, predict and monitor localized failure of such sandwich composites during their service life.

Health monitoring in sandwich composites

Commonly, all three damage modes exist due to low-velocity impact. Facesheet damage is the most obvious from external observation. At the impact site, the facesheet becomes indented. The indentation becomes more visible as the impact energy is increased. As the damage state increases, eventually fiber breakage, matrix cracking, and delamination become evident at the surface. Figure 1.2 shows photographs of a sandwich composite specimen after two strikes at 3.33 J of impact energy per strike. After testing, the specimen is cut in half through the impact site so the interior of the specimen can be seen. Externally, there is little visible damage on the impacted surface other than a small indent and slight discoloration of the surface. In the cross section, however, a fairly large void measuring 17 mm in diameter and 2 mm deep is visible between the faceplate and the crushed core. Furthermore, shear cracks in the core can be readily seen.

Because core crushing and facesheet-core debonding are the dominant modes of failure and because they exist at low impact energies and are unseen by visual inspection, non-destructive health monitoring systems must be developed to assure the safe operation of sandwich composite structures in real world applications. Full-field inspection methods such as infared thermography and surface interferometry, both ultrasound and speckle, have been effectively applied to image damage in composite laminates (Maldague, 2001). However, sandwich composites present difficulties for these conventional measurement systems due to the extreme difference in material properties between the core and facesheet materials. For example, in infrared thermography the strong thermal reflections at the core-facesheet interface prevent the detection of small changes in the interface conditions or damage at other locations. Additionally, these conventional inspection techniques can only be performed during maintenance of the structural component when an operator has access to the component. As such, an in-situ non-destructive evaluation method would be beneficial.

Optical fiber Bragg grating sensors offer a potential in-situ inspection solution (Garret *et al.*, 2009; Propst *et al.*, 2010). They are easy to embed in a laminated structure without perturbing the structure itself, can be quickly interrogated with a laser system, and yield accurate strain readings. Balageas *et al.* (2000) embedded optical fibers with FBG sensors at the facesheet-core interface of foam core sandwich composites to measure the strain in the plane of the interface throughout the lifetime of the composite. The composites were subjected to multiple low-velocity impacts while the permanent strain after each impact was measured from the peak wavelength response of the FBG sensor. During the impact events, a rapid strain increase was measured, followed by a relaxation phase. The authors observed that the change in permanent residual strain correlated to the increase damage (independently measured with ultrasonic and shearographic imaging), however the correlation was not strict.

One of the unique characteristics of FBG sensors is the richness of information that can be extracted from the full-spectral response of the sensor when peak-tracking interrogation is not applied. Minakuchi *et al.* (2007) embedded FBG sensors at the facesheet-core adhesive bond in honeycomb core sandwich composites and demonstrated that the FBG response spectrum was highly distorted due to the non-uniform residual stresses in the adhesive after curing at elevated temperatures. The authors therefore detected debonding at the facesheet-core interface by the release of these non-uniform stresses which returned the FBG spectrum to the undistorted state. While this non-uniform residual stress is not expected at the facesheet-core interface in foam core composites, transverse compressive effects are expected to produce similar distortions in the FBG spectral response. Minakuchi *et al.* (2009) also extended this concept to Brillouin based scattering measurements in an optical fiber without FBG sensors, for which the non-uniform residual strains caused broadening of the scattered frequency spectrum which was also removed when debonding occurred.

In this thesis, we investigate the response of embedded FBG sensors at the core-facesheet interface of sandwich composite structures consisting of carbon fiber reinforced polymer (CFRP) faceplates and a foam core. By measuring both the peak wavelength response of the FBG during impact and the full-spectral response of the FBG during residual strain states, we evaluate the utility of these sensors for damage identification.

CHAPTER 1 FIGURES

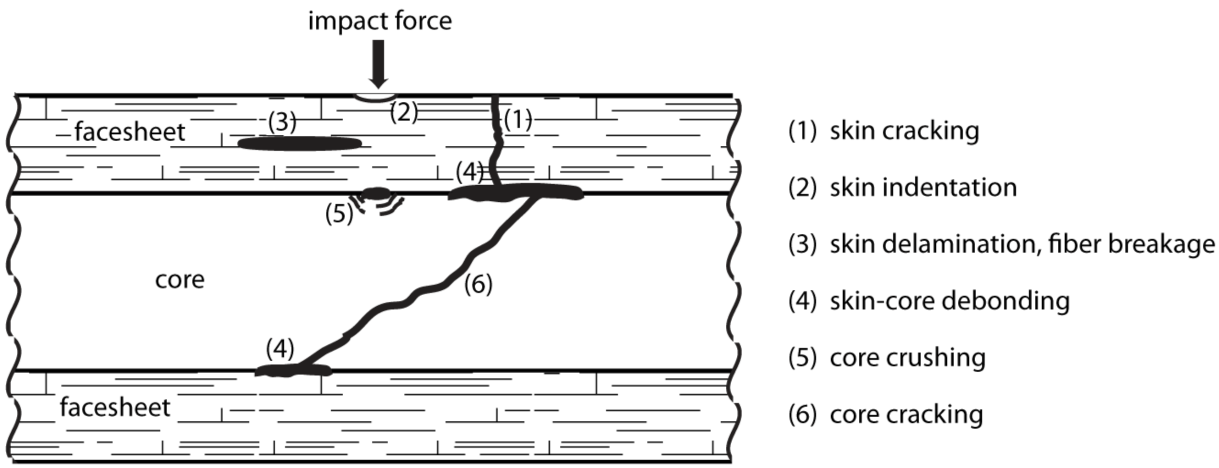

Figure 1.1. Experimentally observed damage modes in a sandwich composite under low velocity impact.

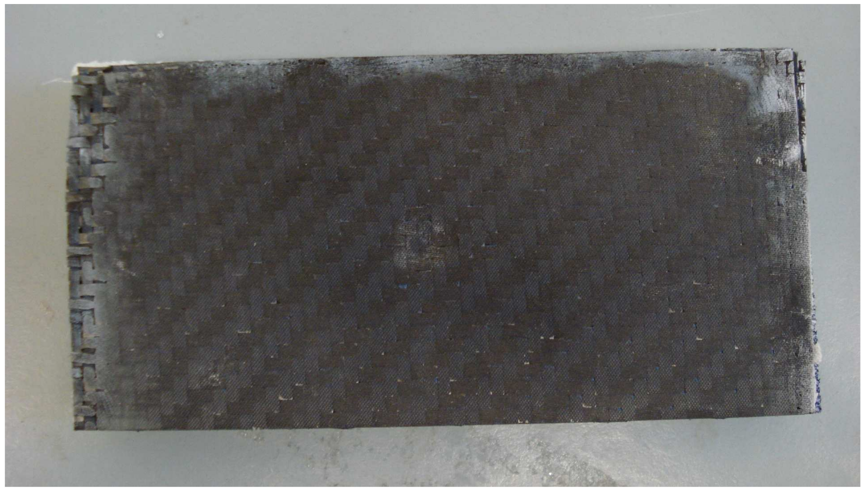

(a)

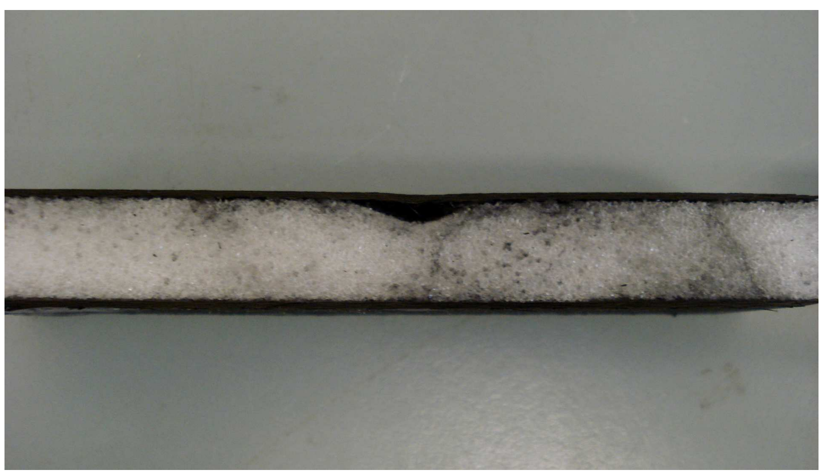

(b)

Figure 1.2. Photographs of impact damage in woven graphite-fiber epoxy facesheet - Rohacell foam core sandwich composite after low-velocity impact. (a) view of impacted surface; (b) view of cross-section.

CHAPTER 2. EXPERIMENTAL METHODS

Specimen Fabrication

The facesheets for the specimens were two identical 11.43 cm square plates of a two dimensional twill woven carbon fiber prepreg with a thermoset matrix (Advanced Composites LTM22/CF0300). Each facesheet was assembled from four pre-preg layers, all stacked in the same orientation. The facesheets were first assembled between sheets of peel ply and enclosed in a mylar vacuum bag sealed by plumber's putty. The two facesheets were cured in the same vacuum bag at the same time, separated by four additional sheets of peel ply. A vacuum was drawn in the bag, then the bag was sealed and put into a hotpress. The laminate underwent the three stage temperature curing cycle shown in Fig. 2.1. A constant pressure of 8.27 MPa was applied to the laminate throughout the cure cycle. Figure 2.2 presents a schematic of the assembly process.

The sandwich composite specimen cores consisted of Rohacell IG 71 foam of thickness 1.27 cm. Rohacell IG 71 is a commonly used aerospace foam of medium density. The foam was bonded to the facesheets using a medium thickness cyanoacrylate (CA) glue that achieves most of its bonding strength in the first ten seconds, and full bonding strength in under 2 hours. Once the CA glue was applied, the facesheets and core were left under a pressure for 10 minutes to assure a complete bond. If optical fibers were to be embedded in the sample, they were placed at the core-facesheet interface when the facesheets were bonded to the core. The optical fibers were placed 1.27 cm from the point to be impacted, located at the center of the specimen. Once the sandwich composite had been manufactured, it was cut in half with a wet saw to produce two identical 11.43 x 5.72 cm samples. No visible damage was present after the specimens were cut. The dimensions of the completed specimen are shown in Fig. 2.3.

Low velocity impact loading

Once manufactured, the specimens were subjected to low velocity impact testing. Each specimen was mounted in an impact tower capable of delivering impact energies between 1 J and 500 J. The impactor consists of an aluminum crosshead with a 19mm diameter spherical indenter. The entire assembly had a mass of 5.5. kg. A photograph of the drop tower is shown in Fig. 2.4. The composite laminates were securely clamped by a 76.2 mm inner and 152 mm outer – diameter circular steel ring sandwiched by a neoprene mat to distribute pressure evenly over the boundary. The specimens were securely clamped by hand tightening each of the four nuts until the specimen was secure without causing crushing of the foam core. Each specimen was repeatedly impacted with an impact velocity of 1.1 m/s until perforation of the impacted facesheet. An image of an impacted facesheet after failure can be seen in Fig. 2.5. The rebound of the crosshead was manually arrested to prevent rebound impacts during a single strike event. Throughout each impact event the acceleration of the impactor was collected from a piezoelectric accelerometer mounted on the crosshead and the position of the impactor was obtained from a non-contacting magnetorestrictive sensor on the guide rail. Both sensors were interrogated with an oscilloscope at 50 kHz and triggered by the position sensor at a fixed distance above the specimen surface height. This height measurement was recorded after each strike by resting the crosshead on the specimen surface. The impactor contact force profile was determined from the accelerometer and filtered using a 0.46 millisecond moving average. From this filtered contact force, the maximum contact force was calculated for each strike.

Using the slope of the position data curve, pre-impact and post-impact velocities were calculated. These values were used to determine the energy dissipated by the specimen for each strike, ΔKE,

$$\Delta KE = \frac{1}{2} m (v_{in}^2 - v_{out}^2) \tag{2.1}$$

where v_{in} is the pre-impact velocity, v_{out} is the post-impact velocity and m is the mass of the impactor (5.5 kg).

Twelve specimens were impacted without an embedded optical fiber. From the acceleration and position data, input velocity, output velocity, maximum contact force, and dissipated energy were calculated for these specimens (Pearson *et al.*, 2009). Next, ten specimens with an embedded fiber were submitted to the same low velocity impact test as those without embedded fibers. The optical fibers in these ten specimens did not have FBG sensor. This set of specimens was used to determine how the presence of an optical fiber affected specimen lifetime and response. Finally, four specimens were tested with an embedded optical fiber that did contain an FBG sensor.

Fiber Bragg grating sensor interrogation

The optical fiber embedded in the sample was cleaved using a CT-07BS High Precision Cleaver from Fujikura. The cleaver creates a clean, 90° cut at the end of the fiber which allows the fiber to be spliced to another fiber. An Ericsson FSU 975 Fusion Splicer was used to splice the leads embedded in the specimen to a fiber optic patch cable which was then connected to a Micron Optics si720 laser for interrogation. The Micron Optics si720 is a dynamic swept tunable laser for interrogation of the FBGs in reflection. Therefore, only one of the two leads coming out of each specimen needed to be spliced. The Micron Optics si720 interrogator can perform both peak wavelength (at kHz) and full spectral (1 Hz) scanning of the FBG. The peak wavelength was recorded during each strike at 1 kHz, while the full spectral response was recorded between strikes once the laminate had reached equilibrium.

FBGs are written into the core of an optical fiber and act as a transmission filter, reflecting a narrow wavelength bandwidth of light. The wavelength at maximum reflected intensity is referred to as the Bragg wavelength for the FBG. As the optical fiber is stressed axially, the reflected spectrum shifts in wavelength. This shift is to higher wavelengths for axial tension and to lower wavelengths for axial compression. Using Equation 1.1, the axial strain on the fiber can be calculated from the peak (Bragg) wavelength shift,

$$\varepsilon = \frac{\Delta\lambda}{\lambda_B(1-p_e)} \tag{2.2}$$

where $\Delta\lambda$ is the change in peak wavelength, λ_B is the original, unstressed peak wavelength, p_e is the effective strain-optic coefficient for the optical fiber fundamental mode, and ε is the strain. For the optical fibers used in this experiment (Corning SMF-28) p_e was calibrated to be 0.22. When non-uniform axial strains or transverse stress components are applied to the optical fiber, the reflected spectrum of the FBG is no longer a simple reflected peak. The reflected spectrum can broaden or take the form of multiple peaks or a more complex spectral form.

Infrared thermography

For independent comparison, the damage in some specimens was imaged using transient infrared thermography. The specimens were removed from the drop tower and imaged from both the impacted (top) surface and from the side after each strike. The specimens were held in place in an aluminum frame by a Rohacell plate to reduce heat transfer from the specimen to the aluminum rails. The specimens were imaged from the front of specimen and the images were captured from the infrared camera (Cedip Infrared Titanium) using a PC and Altair software. A copper plate heating system was used to heat the specimens from the rear. The copper plate was heated by water at an elevated temperature flowing through the copper tubing, soldered to the back of the plate. The water temperature was raised to 50 °C in a separate, temperature controlled bath and circulated through the copper tubing. For this transient (slow-speed) thermography, the specimens were heated until they had reached equilibrium, at which point the image acquisition began and the heating system was removed from the back of the specimen.

CHAPTER 2 FIGURES

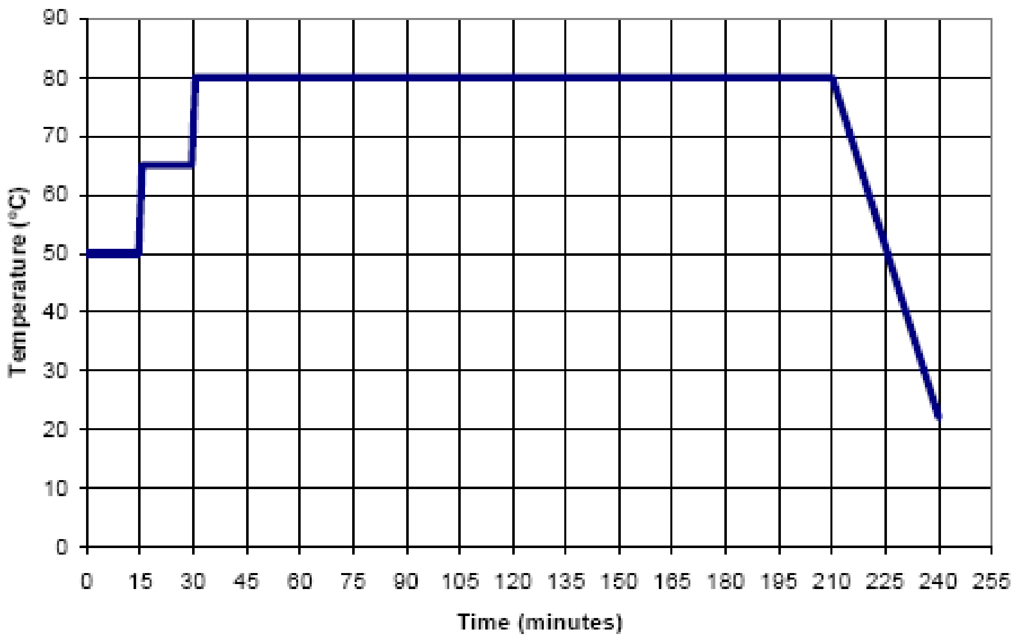

Figure 2.1. Temperature cure cycle for specimen fabrication.

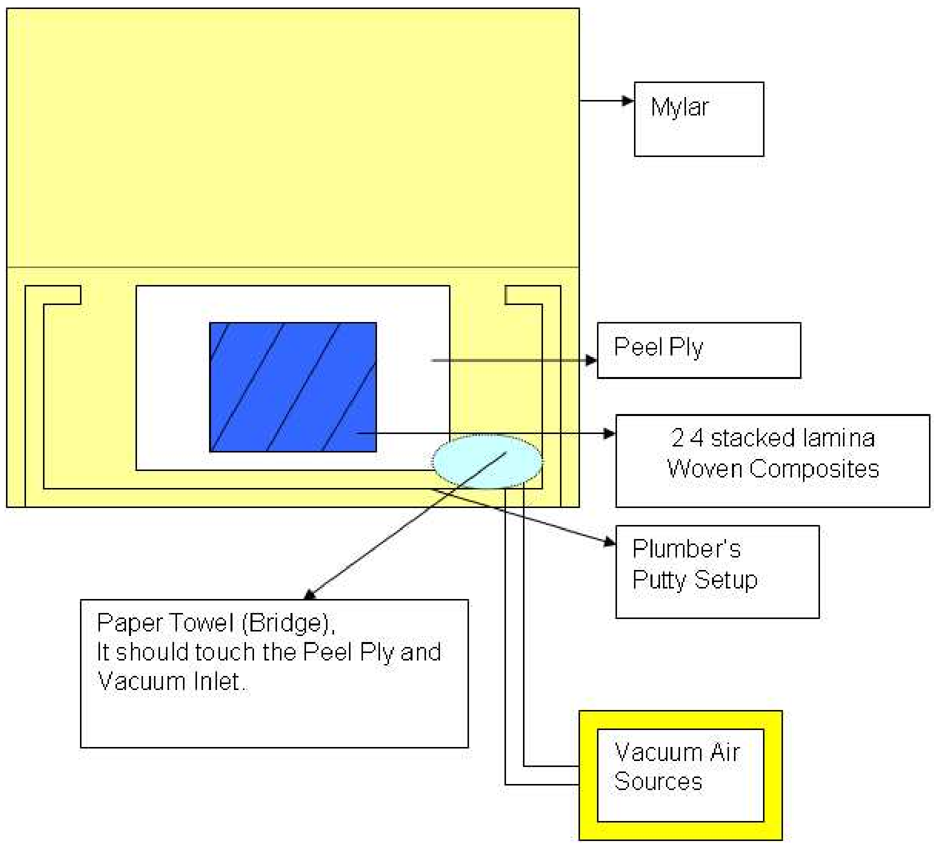

Figure 2.2. Schematic of pre-preg laminate layup and vacuuming bagging arrangement.

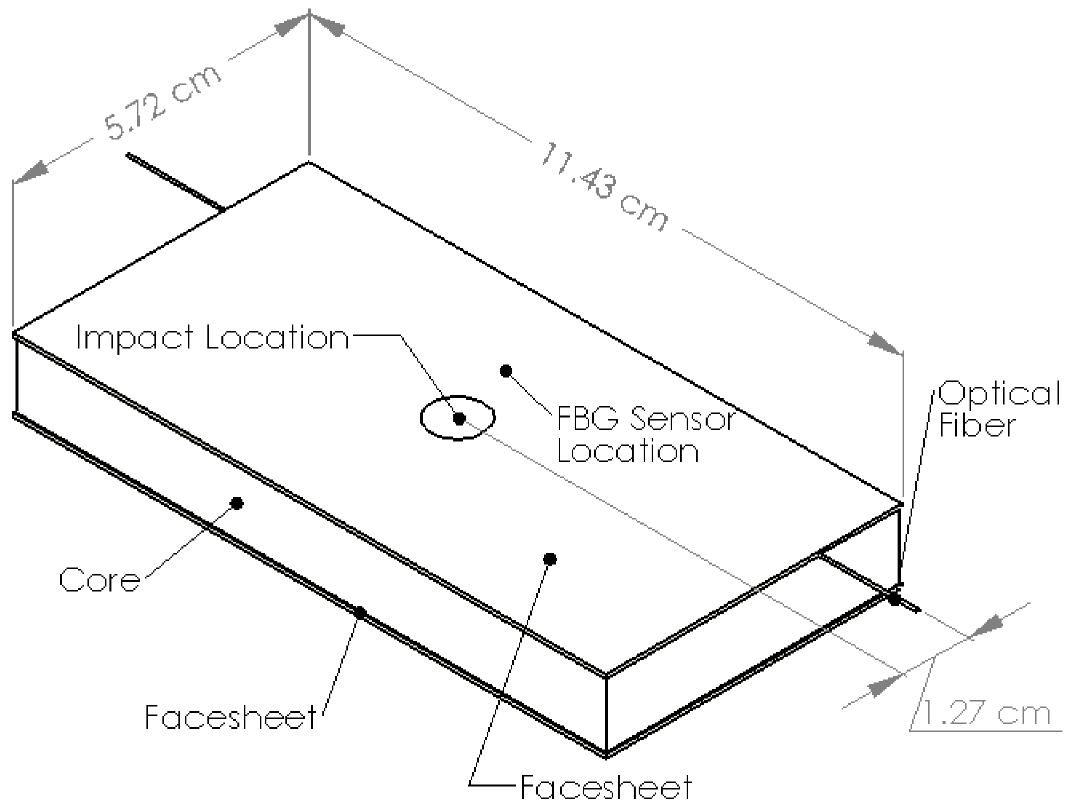

Figure 2.3. Schematic of sandwich composite specimen dimensions with location of embedded optical fiber and FBG sensor.

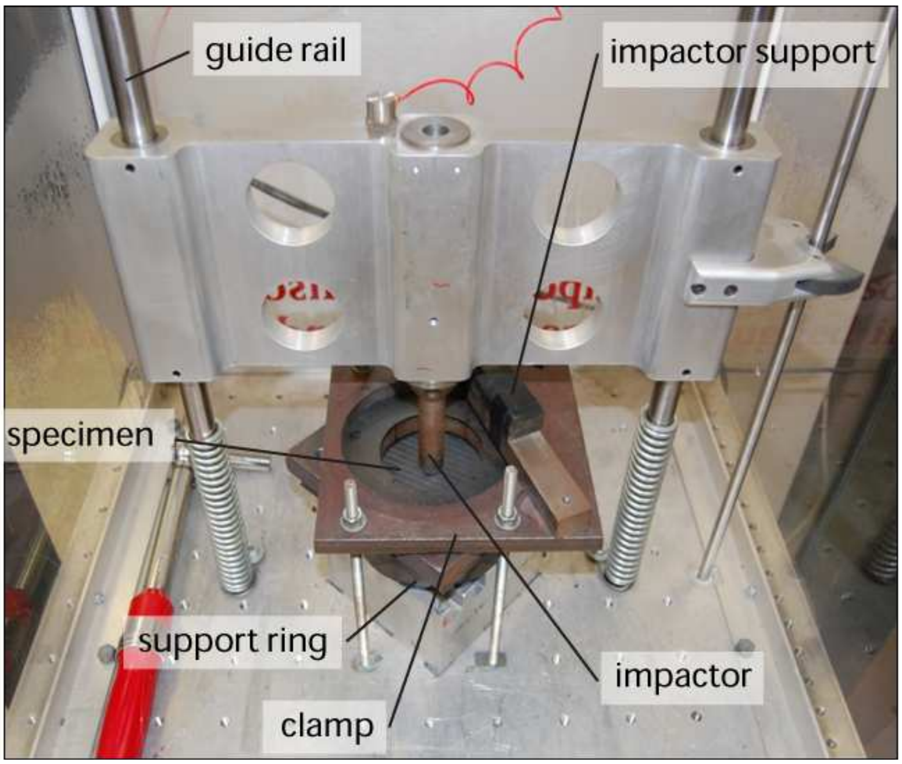

Figure 2.4. Photograph of drop tower.

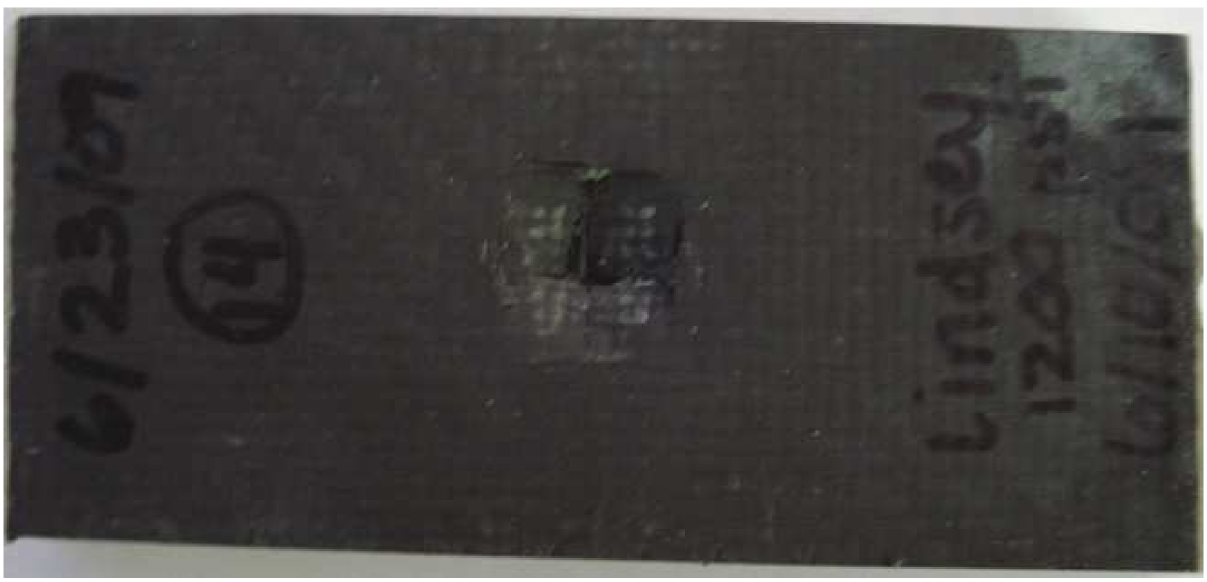

Figure 2.5. Impacted facesheet of specimen showing perforation by impactor.

CHAPTER 3. RESULTS AND DISCUSSION

Infared Thermography

Figures 3.1-3.3 present infrared thermography images of a specimen (11) after various strikes. This specimen survived 22 strikes before failure. The figures were taken of both the impacted surface and the side of the specimen. Damaged areas of the specimen at the facesheet core interface trap heat and therefore cool at a different rate than undamaged regions; therefore the resulting thermography images highlight damage in the specimen. Similarly, cracks in the foam also propagate heat though the specimen at different rates than the surrounding foam.

Figure 3.1 was taken after a single impact to the specimen. The thermographic image does highlight a small amount of facesheet indentation; however, the system is unable to penetrate the facesheet and determine if there is any damage at the core-facesheet interface. The side view is also inconclusive. Figure 3.2 was taken approximately halfway through the lifetime of the specimen. Similar to Fig. 3.1, the thermography images highlights the facesheet indentation and matrix cracking that are also visible in the photograph of the specimen surface. The thermographic system is once again unable to penetrate the top facesheet and give an impression of the core or core-facesheet interface damage. The side view, however, does show obvious shear cracking in the core which is barely visible in the photograph. More importantly, the photograph of the side of the specimen shows considerable debonding between the facesheet and the core. This debonding is expected to be present as indicated by the core shear cracks and the extended matrix cracking across the facesheet. Figure 3.3 was taken at the end of the specimen lifetime. The facesheet image shows the same failure as that of Fig. 3.2, however the size of the facesheet indentation has increased. Based on Figure 1.2, extensive core crushing is present in the foam at this point, however this cannot be seen from either the thermography images or photographs of Fig. 3.3. As core crushing is an important source of reduced strength of the composite, these images highlight the need for embedded, in-situ sensor measurements and the localized level of strain information that must be obtained.

Infrared thermography was not used to image all specimens, because the removal of the specimen from the testing fixture did compromise the integrity of the impact testing. It is important to impact the specimen at the same location during every strike, and because the specimen was unclamped under each strike this is not assured. The faceplate failure of the specimen that underwent thermography is different than the others tested. Most failed in the same way as the specimen in Figure 2.5: a pyramid shaped indentation with four cracks. This specimen, as shown in Figure 3.3, did have an indentation, but also contained a crack that ran the entire width of the specimen through the impact location. The facesheet-core disbond was also exaggerated in this specimen. Also, the mechanical response of the structure to the repeated heating and cooling cycle necessary for thermography has not been analyzed. For these reasons, infrared thermography was also not applied to the specimens with embedded optical fiber sensors

Specimens Without Embedded Optical Fibers

To determine the response of the sandwich composite structures to low velocity impact, twelve specimens were manufactured without embedded optical fibers and tested until failure. Table 3.1 shows the number of strikes each specimen survived until failure. While the average specimen survived 25 strikes to failure, as expected, there was a large amount of scatter in specimen life. Sandwich composites are able to fail through several different modes and are therefore highly sensitive to local changes in the microstructure including the facesheet-core adhesive bond. Although final failure was defined as perforation of the impacted facesheet, extensive delamination can occur prior to perforation as the specimens were still held together by the clamped boundary conditions. If the delamination exists in the specimen at the impact location, the energy will be partially dissipated through the movement of layers, rather than further damage to the sample itself.

One method to compare the performance of different specimens is to compare the maximum contact force and energy dissipated per strike. Despite the scatter in number of strikes to failure, the behavior of these parameters was similar between specimens. Fig. 3.4 plots maximum contact force vs. strike number and Fig. 3.5 plots dissipated energy vs. strike number for Specimen 1. These plots are characteristic of the response shown by other specimens. The response of other specimens can be seen in the Appendix.

For a constant impact energy, the maximum contact force of each strike generally showed a slight decrease as the damage in the sandwich composite increased because the stiffness of the specimen decreased. The duration of impact therefore also increased. The maximum contact force of each strike was between 1 kN and 1.6 kN for all specimens. The decrease in maximum contact force was not as significant as that seen in laminated composites, as the impact velocities supported are lower and the properties of the foam core contribute significantly to the impact contact force. Crushing of the foam core did not significantly increase the stiffness of the core.

Figs. 3.6 and 3.7 plots the measured, unfiltered contact force history during strikes 2 and 22 respectively for specimen 1. Previous researchers had observed a drop in the contact force history when certain failure modes occurred (Caprino and Teti, 1994; Anderson and Madenci, 2000). Caprino and Teti (1994) observed a drop in contact force during fiber fracture in the impacted facesheet. On the other hand, load drops were not observed due to facesheet-core delamination or core cracking since their effect on the sandwich composite rigidity was negligible. For the impact testing in this work, we do not expect to see the large drops in contact force, as failure was initiated by repeated, smaller impact energies rather than a single impact at a relatively large impact energy. In Fig. X we do observe that early damage in the composite is indicated by large oscillations in the contact force profile, indicative of fiber fracture. This is consistent with the visual observations of damage. Towards the end of the composite lifetime, the contact force time history did not have these large oscillations (see Fig. 3.7) as the damage was in the form of core crushing and facesheet-core debonding.

Unlike the maximum contact force calculation, the calculation of the energy dissipated per strike has much more noise. This noise is a result of the errors inherent in transforming the position data to velocity data then squaring the resulting velocity in the calculation for dissipated energy. The amount of energy dissipated per strike increased as the number of strikes increased due to the reduction in sample stiffness. Therefore, v_{out} of the crosshead is decreased so more energy is dissipated by the sample.

Specimens with Embedded Optical Fibers

Fourteen specimens were tested under low velocity impact with an embedded optical fiber located 1.27 cm from the impact location. Of these fourteen specimens, four of them had a FBG in the embedded fiber. Table 3.2 lists the number of strikes to specimen failure and the number of strikes to optical fiber failure for each specimen. Table 3.2 shows that specimens with an embedded optical fiber had a shorter lifetime. The average lifetime of specimens without an embedded fiber was 25.1 strikes, while the average lifetime of specimens with an embedded fiber was 20.0 strikes. This reduction in composite lifetime is an important obstacle towards applying the FBG sensors for in-situ damage identification. Potential mitigation strategies to reduce the impact of the embedded optical fiber on the sandwich composite properties should be explored in future work, for example machining grooves into the foam core such that the optical fibers do not extend as far into the adhesive layer.

The survivability of the optical fibers was also tested in all specimens. For the specimens without FBG sensors, infrared lightwaves were transmitted through the optical fibers and failure was defined when no transmission was present. This failure always occurred within a single strike. Generally, the optical fiber embedded within the specimen survived throughout most of the life of the specimen. In four specimens, the fiber survived the entire specimen life. The fiber in specimen 17 broke within the specimen before testing could begin. Therefore, no data on fiber life is available for specimen 17. On average, the optical fiber survived 83.8% of the life of the specimen. By the time the specimen did fail, damage was obvious to visual inspection from the laminate surface.

Even though the average lifetime of the specimens with embedded fibers was reduced, the stiffness of the sandwich composite was not. Fig. 3.8 plots maximum contact force vs. number of strikes for specimen 15. Fig. 3.9 plots energy dissipated vs. number of strikes for specimen 15. Both these plots have similar shapes to those of specimen 1 and are indicative of all specimens with embedded fibers. Therefore, even though the specimens with embedded optical fibers to have a shorter lifetime, they have a similar response to those without embedded optical fibers. The maximum contact force and dissipated energy plots for the other specimens with embedded optical fibers are in the Appendix.

Fiber Bragg Grating Sensor Response

Specimens 23, 24, 25 and 26 all contained FBGs within the embedded optical fibers. The FBG was located 1.27 cm away from the point of impact to optimize sensitivity to damage and survivability of the sensor. During each impact event, the peak reflected wavelength of the FBG was measured at 1 kHz. When multiple peaks appeared in the FBG reflected response, as will be shown later, the particular interrogated used followed the maximum intensity peak. Fig. 3.10 plots this peak wavelength tracking for the first 9 strikes of specimen 23. After strike 9 the FBG failed and no wavelength response was obtained. A 10 second window was captured around each impact event. For strikes 2, 3, and 5 the window was not triggered correctly, therefore no data is plotted. During each strike rapid increase in wavelength (tensile strain) followed by a rapid decrease in wavelength (compressive strain) can be observed. The complete cycle was not always captured by the peak tracking due to the relative low interrogation speed as compared to the dynamics of the impact event. After the 10 second window, a relaxation period occurred where the FBG and sandwich composite returned to equilibrium which lasted as long as 5 minutes. The presence of this relaxation period can be seen in the wavelength discontinuities between strikes in Fig. 3.10.

Fig. 3.11 plots the residual strain at the core-facesheet interface obtained from the full-spectral scanning of the FBG reflected response between strikes. The measured FBG reflected spectra are plotted in Fig. 3.12. While it is assumed that the reflected spectra are a measure of the axial strain, in fact transverse stress components on the optical fiber result in the peak-splitting behavior that can be seen in some of the spectra of Fig. 3.12. For the case of this peak-splitting behavior, the residual strains were calculated based on each of the two primary peaks using Eq. 2.2. Both of these residual strains are plotted in Fig. 3.11. One of the peaks represents the axial strain plus the transverse compression and one peak represent the axial strain minus the transverse compression. Therefore, the average of the two peaks represents the axial strain and the distance between them the transverse compression. The plot of the residual strain in Fig. 3.11 was divided into three regions, denoted by the colors red, blue and yellow, based on the behavior of the curves. In the first region, the residual strain is increasing and the FBG response remains a single peak. In the second region, the FBG response splits into two primary peaks and the residual strain decreases. In the third region, the FBG response is still split although the distance between the peaks is decreasing and the average axial strain is increasing again.

Fig. 3.13 plots peak wavelength tracking for all strikes of specimen 24. The FBG sensor survived beyond the lifetime of the specimen. In these wavelength tracking results we can clearly see that the residual strain increased until approximately one-half of the composite lifetime and then decreased for the remaining half of the lifetime. The large tensile strains applied to the FBG sensor during each impact event are also visible. Fig. 3.14 plots the residual strain vs. strike number for this specimen obtained from the full-spectral scanning of the FBG sensor. As a large number of spectra were obtained, only selected spectra from this specimen are plotted in Figs. 3.15 and 3.16. Plots of the remaining spectra are found in the Appendix. The residual strain plot for this specimen is divided into only two regions, the first with an increasing residual strain. The second region includes peak-splitting where one peak residual strain gradually decreased and the other increased significantly then also slowly decreased. Photographs of the facesheet damage during selected strikes are correlated with the FBG spectra in Figs. 3.15 (first region) and 3.16 (second region).

Specimen 25 demonstrated a similar behavior to specimen 23. Figs. 3.17, 3.18, 3.19, and 3.20 plot the peak wavelength tracking results, calculated residual strains and selected FBG spectra, along with photographs of the impacted surface, for this specimen. Plots of the remaining spectra are found in the Appendix. While the specimen survived 15 strikes, the FBG sensor only survived through 8 strikes. The plot of residual strain vs. strike number in Fig. 3.18 is divided into two regions, similar to that of specimen 23. The FBG sensor failed presumably before the composite behavior went into the third region of specimen 23.

The final specimen tested was specimen 26. The results for this specimen are plotted in Figs. 3.21, 3.22, 3.23, 3.24, and 3.25. The residual strain plot is divided into three regions, the same regions as the plot for specimen 23 (Fig. 3.11). An important difference between these specimens is the duration of each of the regions, however. When specimen 26 was impact tested, the FBG reflected spectrum split much earlier, on the second strike. However, after strike 4, the spectrum returned to a single peak and by the end of testing there was almost no strain measured by the sensor.

Discussion of FBG Response

Tracking of the FBG sensor peak wavelength at 1 kHz during the impact events gives little indication of the damage state within the sandwich composite. For remote, in-situ damage detection this would be a difficult measurement to obtain because it would require high-speed scanning of the sensor continuously in order to capture all unexpected impact events. On the other hand, full-spectral scanning of the FBG sensor could be performed on regular intervals without the need for continual tracking. This sensor response measurement did provide significant information about the damage state of the sandwich composite throughout its lifetime. From the full-spectral scans, indications of the both the strain in the plane of the adhesive bond and perpendicular to the adhesive bond (related to the peel stress) could be obtained. This large transverse stress component has been previously determined to dominate the failure of the adhesive (Avrashi *et al.*, 1995).

The key to identifying the existence of damage states and the relative condition of the composite is the combination of these two strain components. From the results of specimens 23-26, we can observe the general trend of these two components and there affect on the FBG full-spectral response at critical points in the composite lifetime:

- The first appearance of damage for these specimens was core crushing, as can be seen in Fig. 1.2, obtained after only 2 strikes. In this case, the optical fiber remains bonded to the relatively stiff facesheet and is subjected to pure tension. The FBG reflected spectrum therefore remains as a single peak in tension. This behavior is seen in the first region for all four specimens. This region was extremely short, lasting only 1-2 strikes (except for specimen 24) due to the weak foam core.
- The second damage condition, present as region 2 in all specimens, is characterized by indentation and/or fracture of the facesheet. In this condition, the permanent, residual deformation of the facesheet in the direction of the foam core creates a large transverse compressive stress on the optical fiber. This compressive stress creates peak-splitting in the FBG spectral response. In all specimens except specimen 24, the resultant residual axial strain on the FBG sensor was in compression as this peak splitting occurred. In specimen 24, the axial strain oscillated and then increased rapidly at approximately strike 23. This may have been due to pinching of the optical fiber by the facesheet.
- The third damage condition, observed in specimens 23 and 26, was due to debonding of the core-facesheet interface which released some of the axial stress and transverse compression on the optical fiber. This final damage condition was not observed in specimens 24 and 25 in which the optical fiber may have failed prior to debonding. The best example of this condition is seen

in specimen 26 in which the transverse compression was immediately released after strike 4 and the axial load was slowly released with further impacts.

These results demonstrate the tremendous potential of FBG sensors, embedded at the core-facesheet interface, to identify damage states through in-situ monitoring of sandwich composites. The disparate material properties between the facesheet and core materials, which create significant challenges for conventional non-destructive evaluation methods, enhance the damage detection through large deformations in the core at the impact location. The large flexibility of the foam core creates large deformations with sharp strain gradients at the impact location (Nemes and Simmonds, 1992; Avrashi *et al.*, 1995). One future challenge in applying the FBG sensors would be the localized nature of the core deformation, as sensors located at a distance sufficiently far from the impact location would not be influenced by the localized deformation of the core material (Schubel *et al.*, 2005).

CHAPTER 3. FIGURES AND TABLES

(a) **(b)**

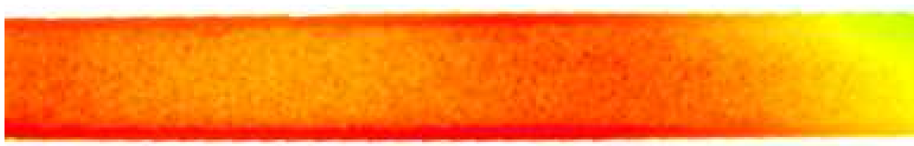

(c)

(d)

Figure 3.1. Infrared thermography image of specimen 11 after strike 1: (a) thermography image of upper facesheet; (b) photograph of upper facesheet; (c) thermography image of cross-section; and (d) photograph of cross-section.

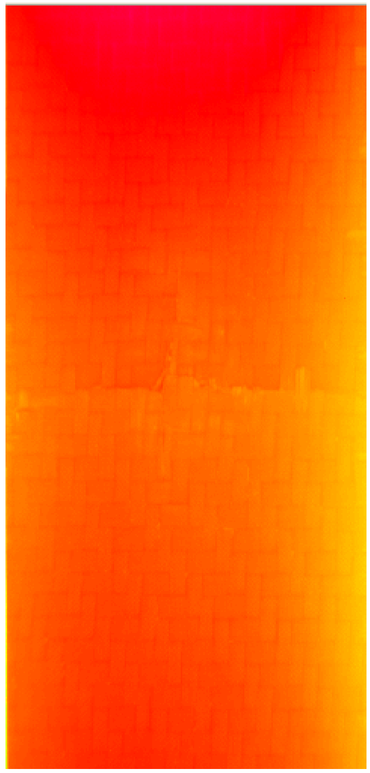

(a) **(b)**

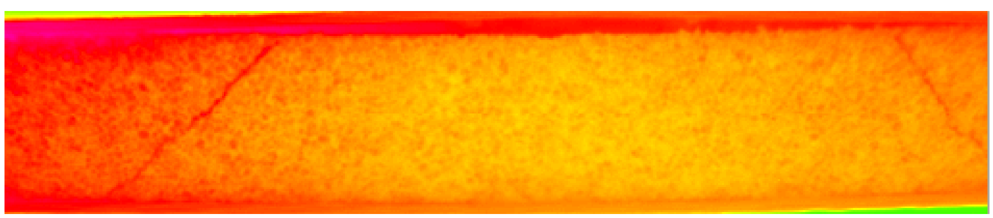

(c)

(d)

Figure 3.2. Infrared thermography image of specimen 11 after strike 16: (a) thermography image of upper facesheet; (b) photograph of upper facesheet; (c) thermography image of cross-section; and (d) photograph of cross-section.

(a) **(b)**

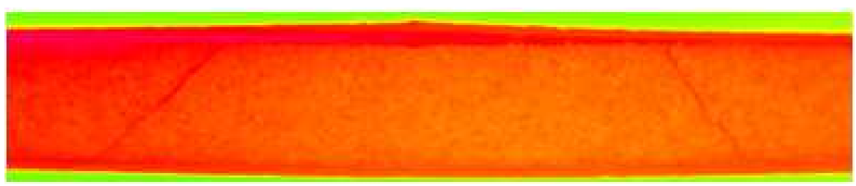

(c)

(d)

Figure 3.3. Infrared thermography image of specimen 11 after strike 21: (a) thermography image of upper facesheet; (b) photograph of upper facesheet; (c) thermography image of cross-section; and (d) photograph of cross-section.

Table 3.1. Table of specimen life for each specimen.

Specimen Number	Number of Strikes to Failure
1	26
2	26
3	39
4	47
5	27
6	25
7	21
8	11
9	16
10	21
11*	22
12	20
Average	25.1

* - Thermography specimen

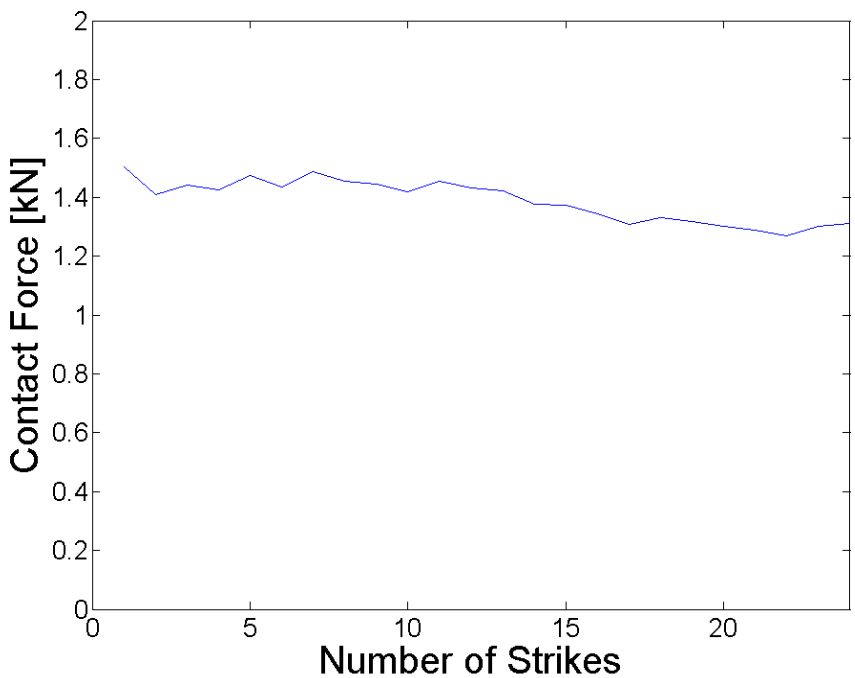

Figure 3.4. Maximum contact force as a function of the number of strikes for specimen 1.

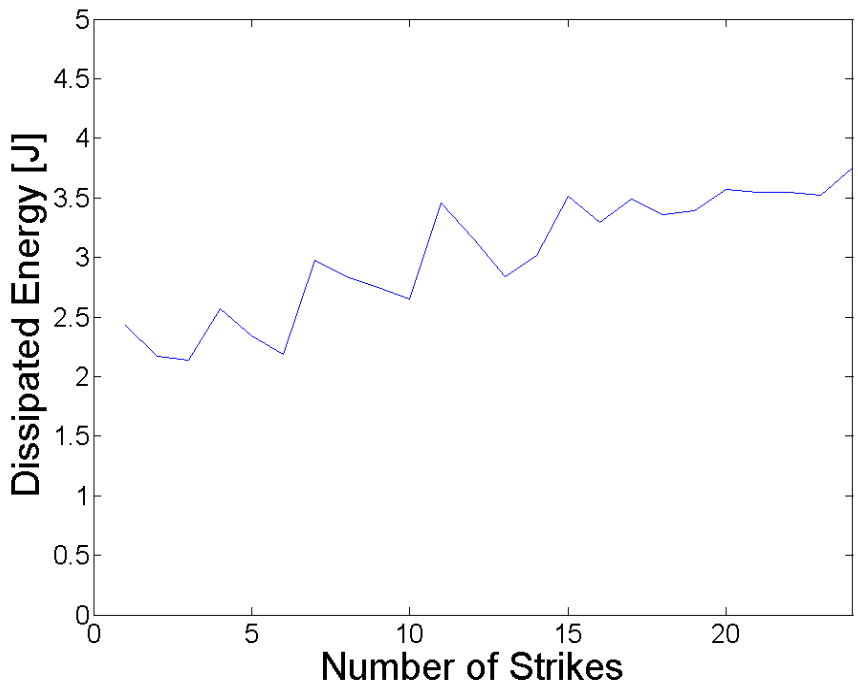

Figure 3.5. Dissipated energy as a function of the number of strikes for specimen 1.

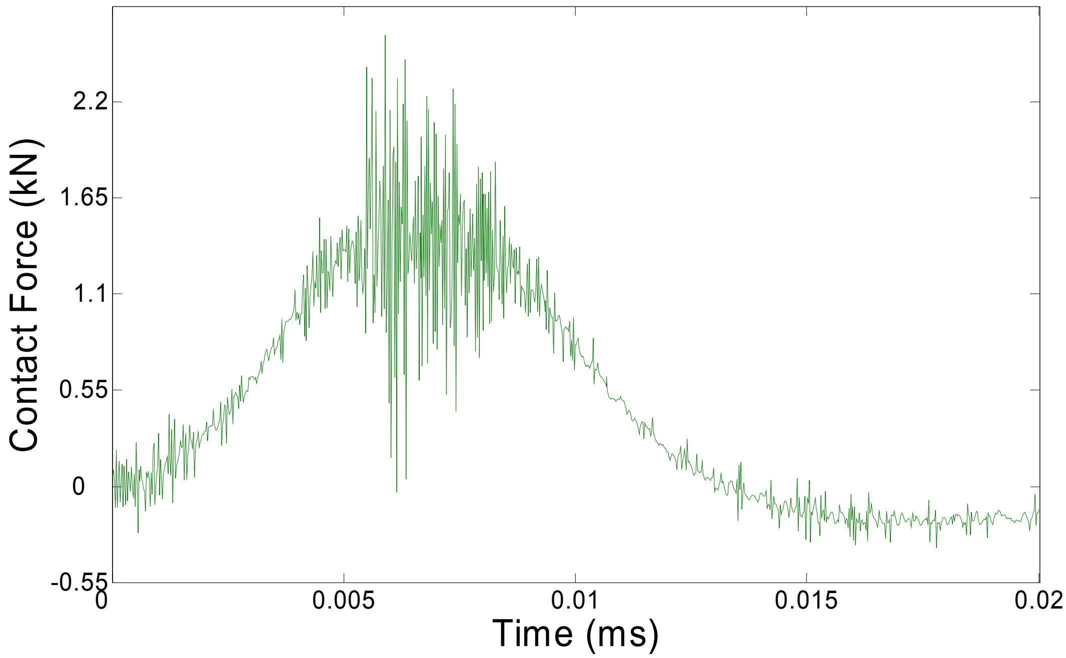

Figure 3.6. Contact force plot for strike 2 from specimen 1.

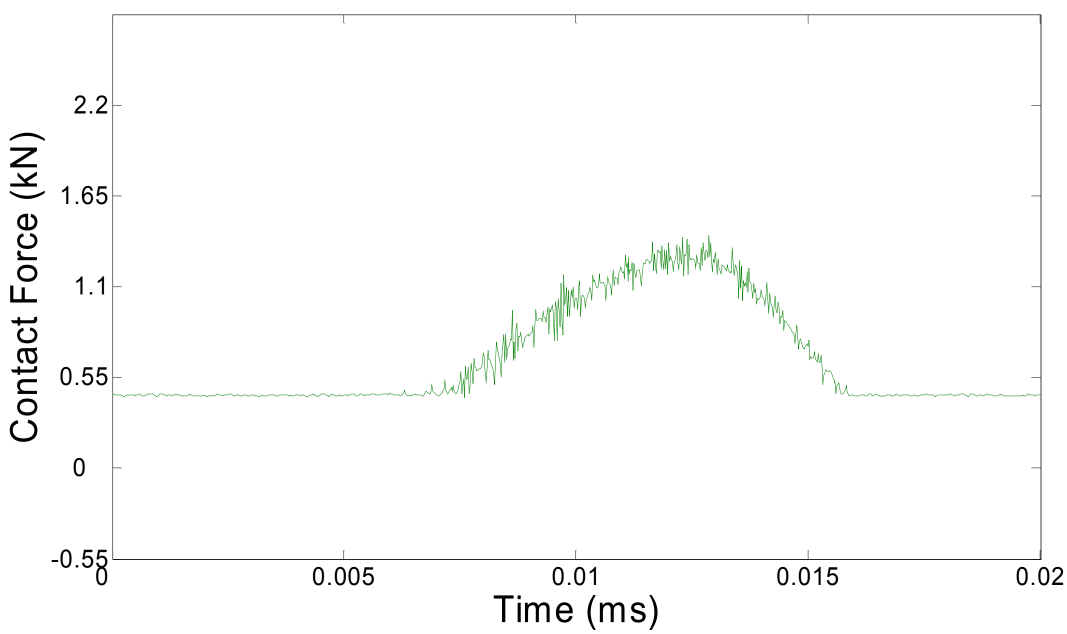

Figure 3.7. Contact force plot for strike 22 of specimen 1

Table 3.2. Lifetime of specimens with embedded optical fibers

Specimen Number	Number of Strikes to Failure	Number of Strikes to Fiber Failure	Fiber Life (%)
13	11	9	81.8
14	24	14	58.3
15	25	21	84
16	23	23	100
17	12		
18	6	3	50
19	21	21	100
20	48	48	100
21	5	4	80
22	10	10	100
23*	22	9	40.9
24*	38	38	100
25*	15	8	53.3
26*	20	20	100
Average	20.0	17.5	80.6

* - Embedded FBG

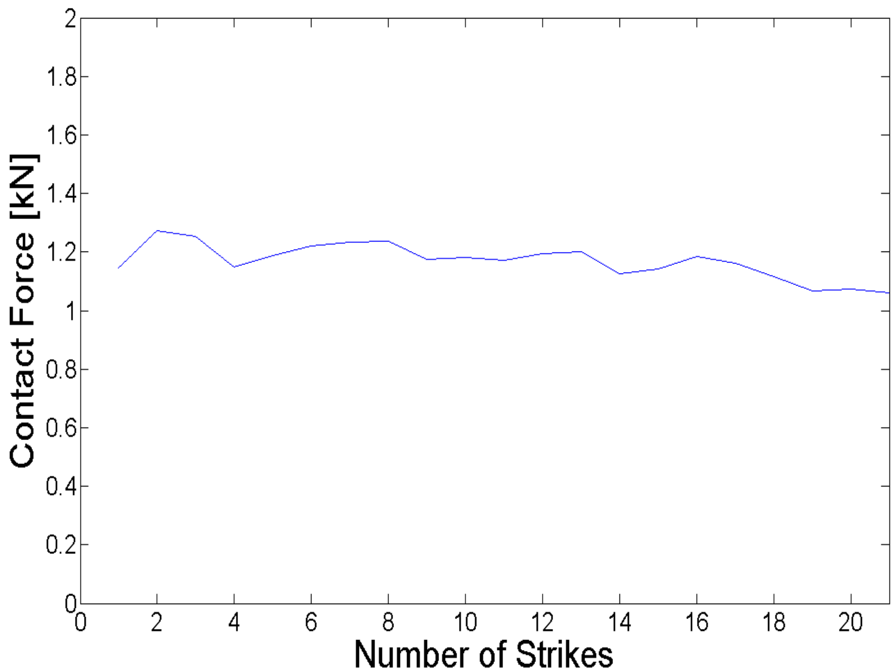

Figure 3.8. Maximum contact force as a function of number of strikes for specimen 15.

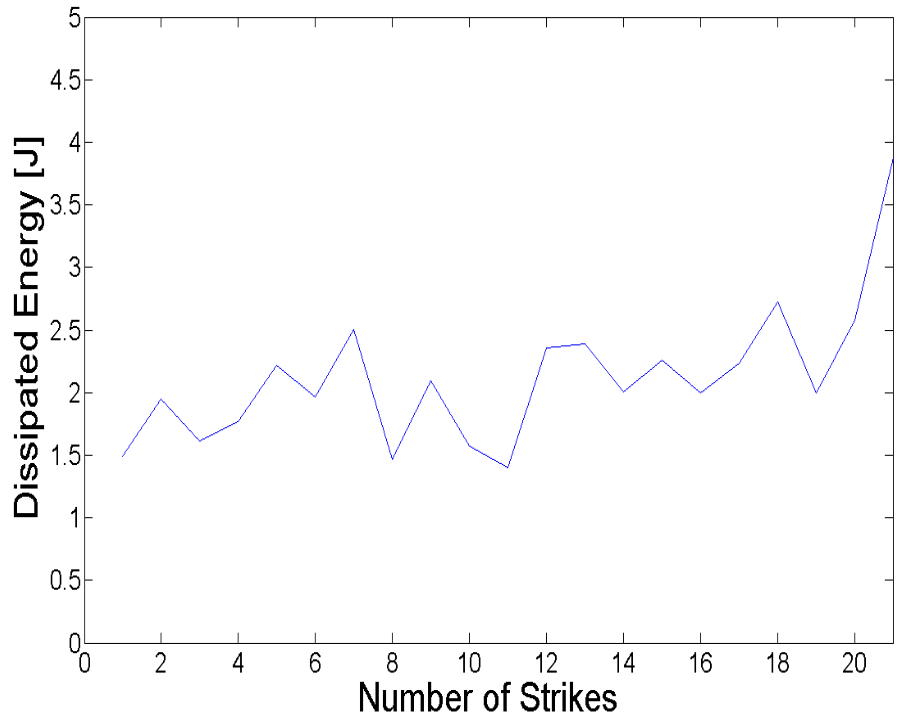

Figure 3.9. Dissipated energy as a function of number of strikes for specimen 15.

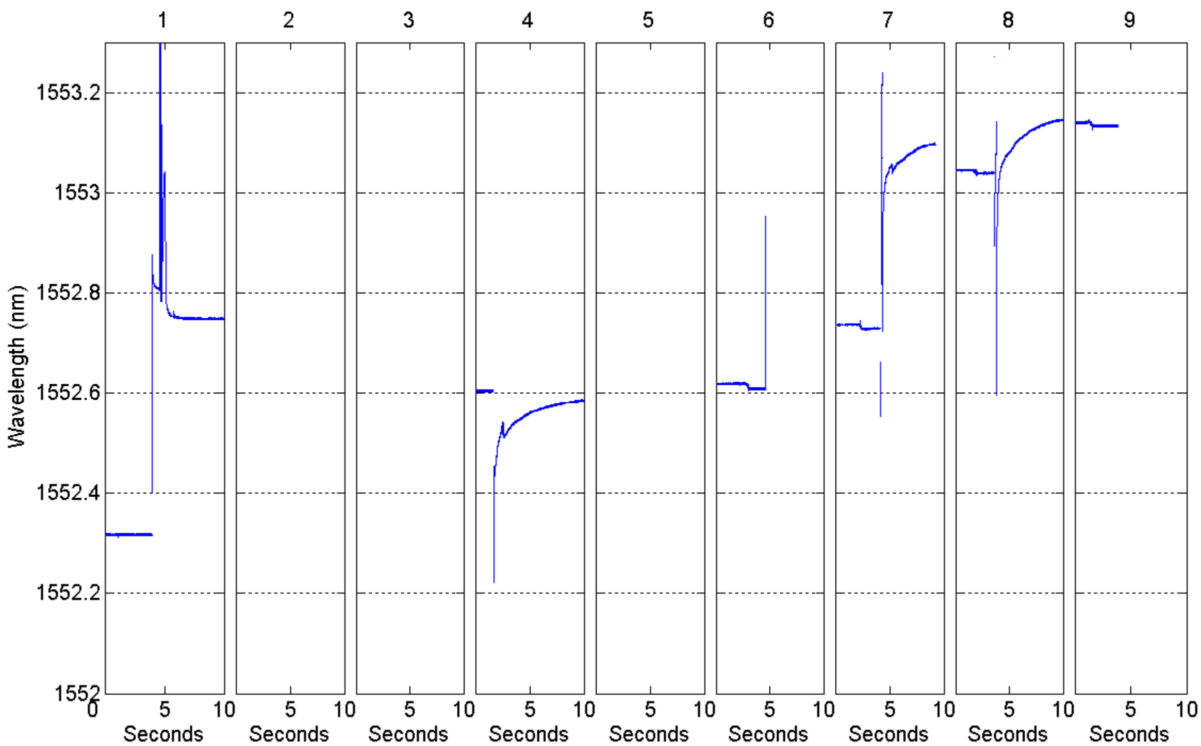

Figure 3.10. Peak wavelength change per strike of specimen 23.

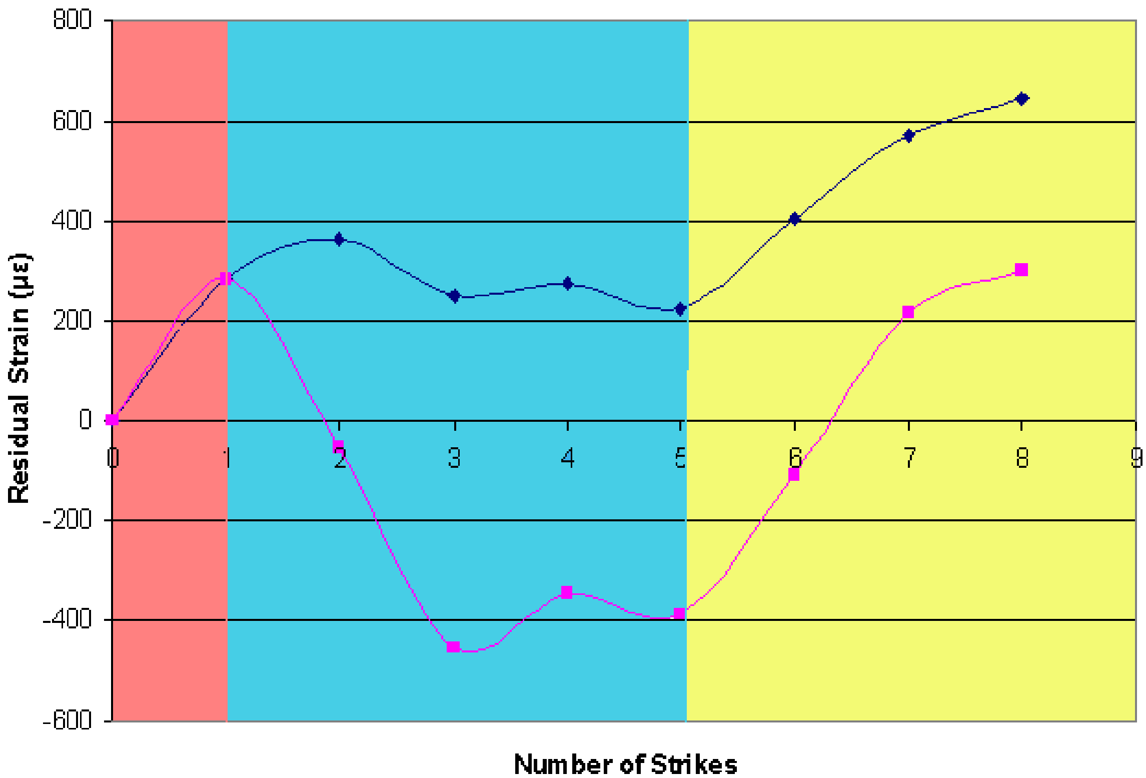

Figure 3.11. Residual strain plot for specimen 23 divided into three regions.

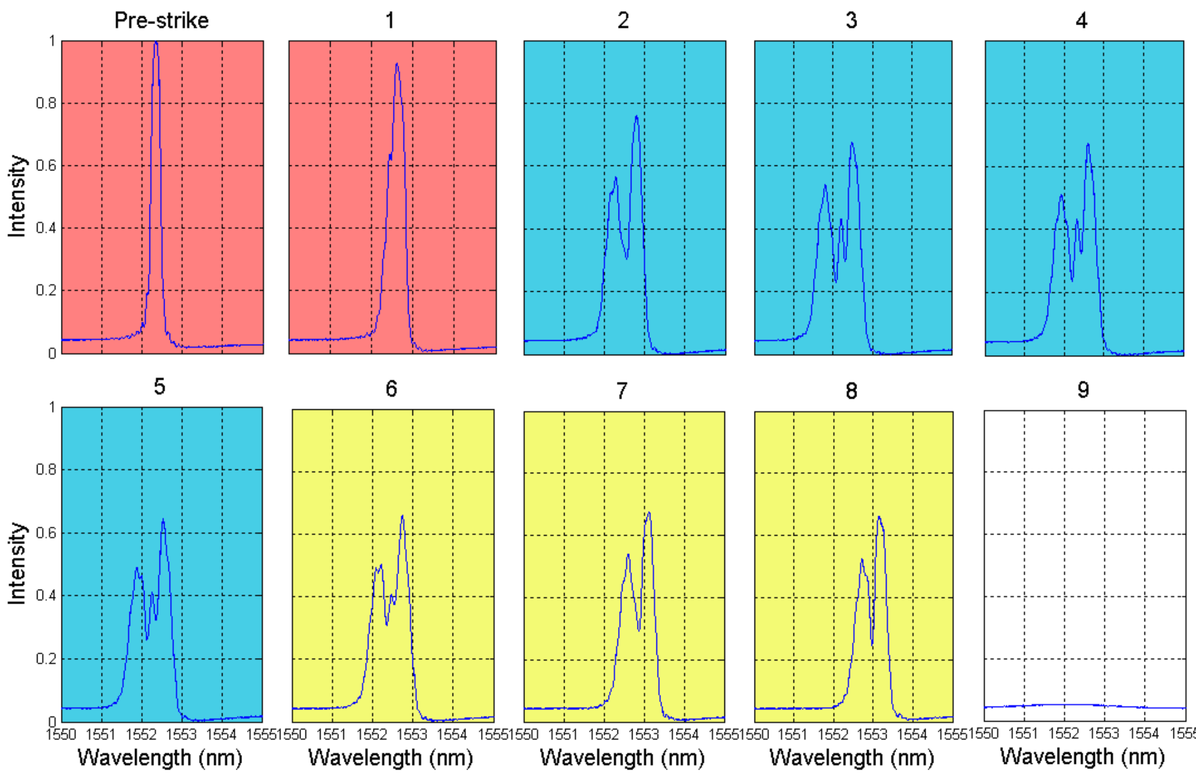

Figure 3.12. Spectral sweep after each strike for specimen 23.

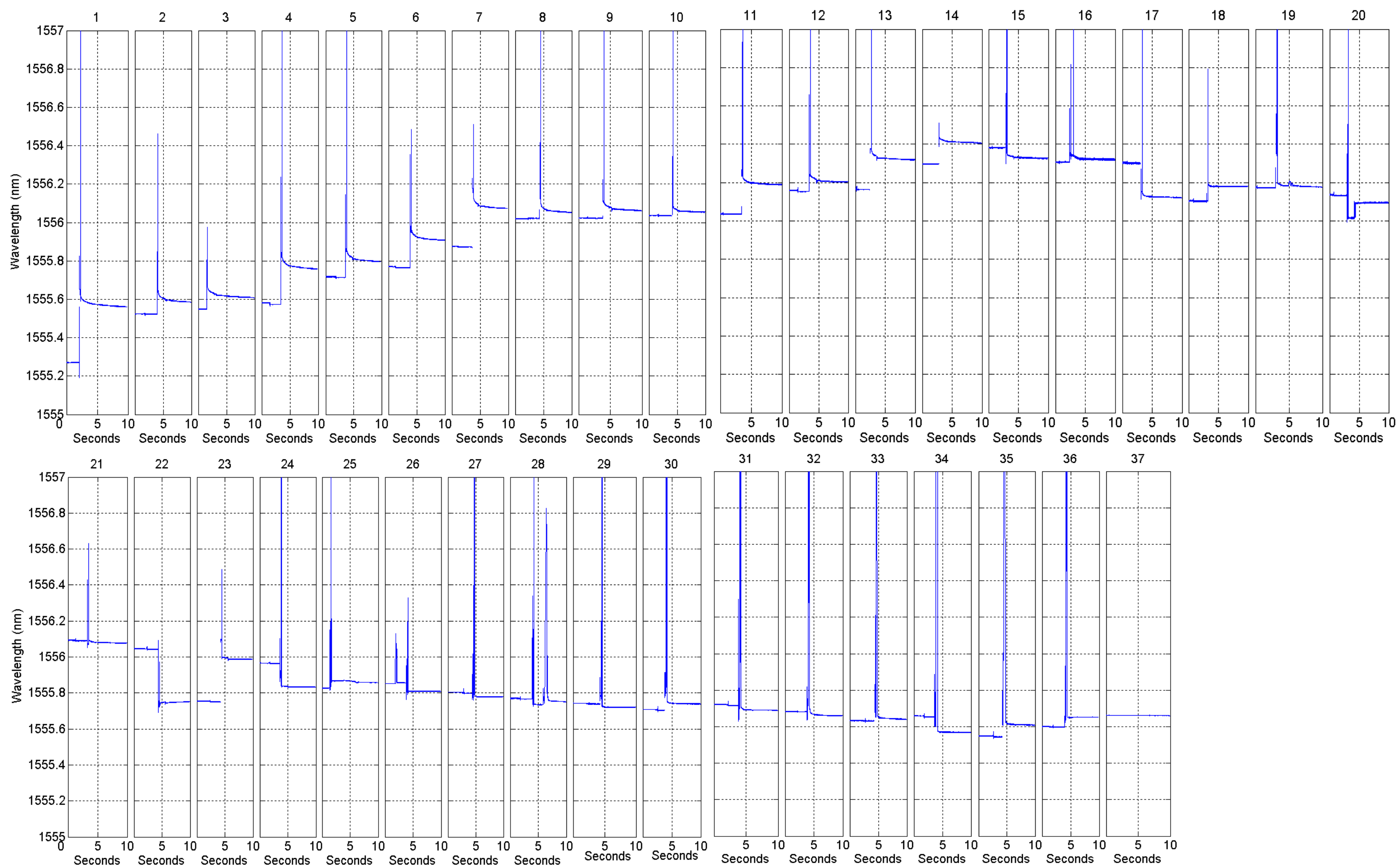

Figure 3.13. Peak wavelength change per strike of specimen 24.

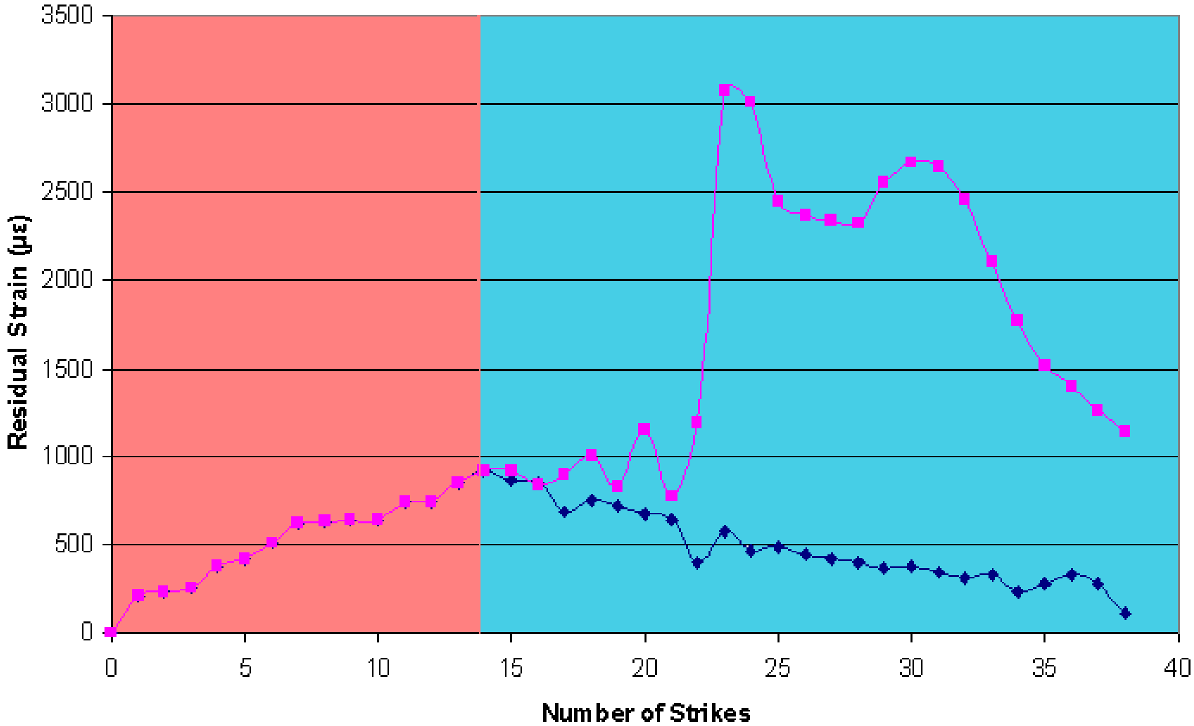

Figure 3.14. Residual strain plot for specimen 24 divided into two regions.

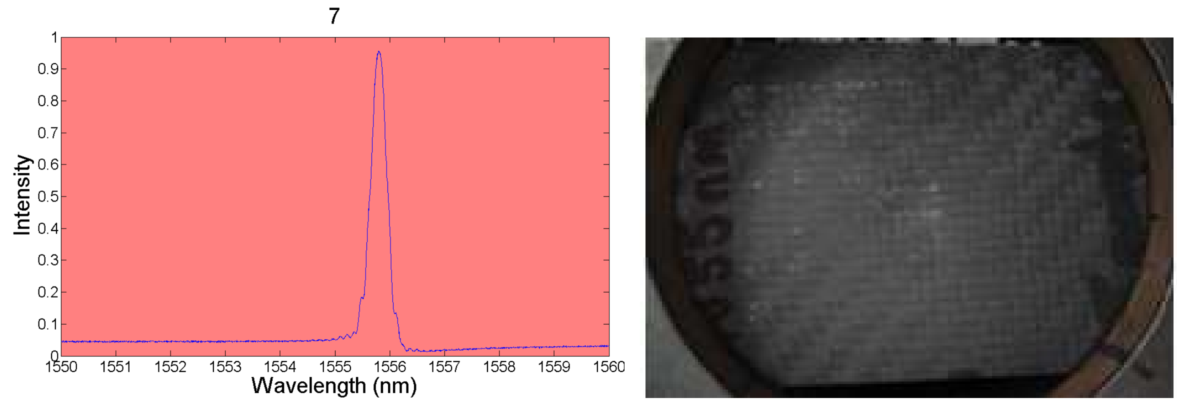

(a)

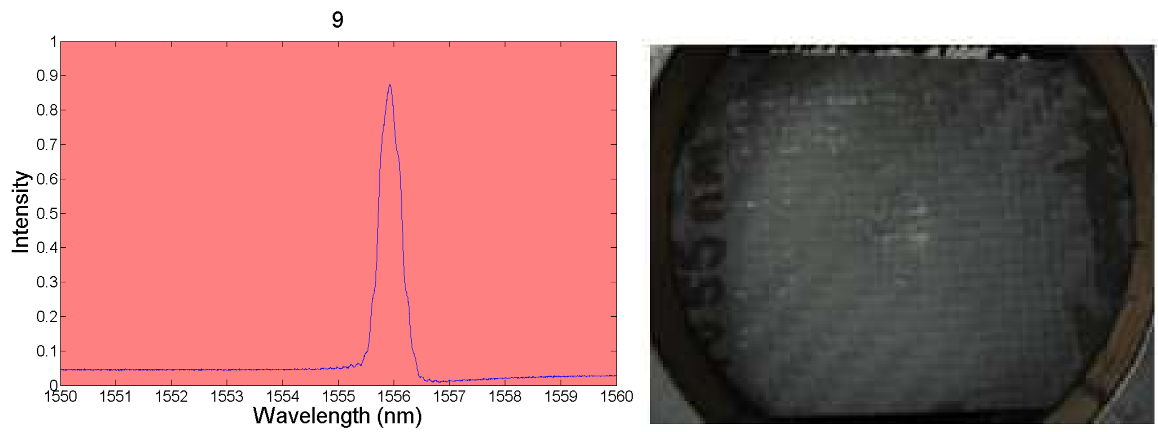

(b)

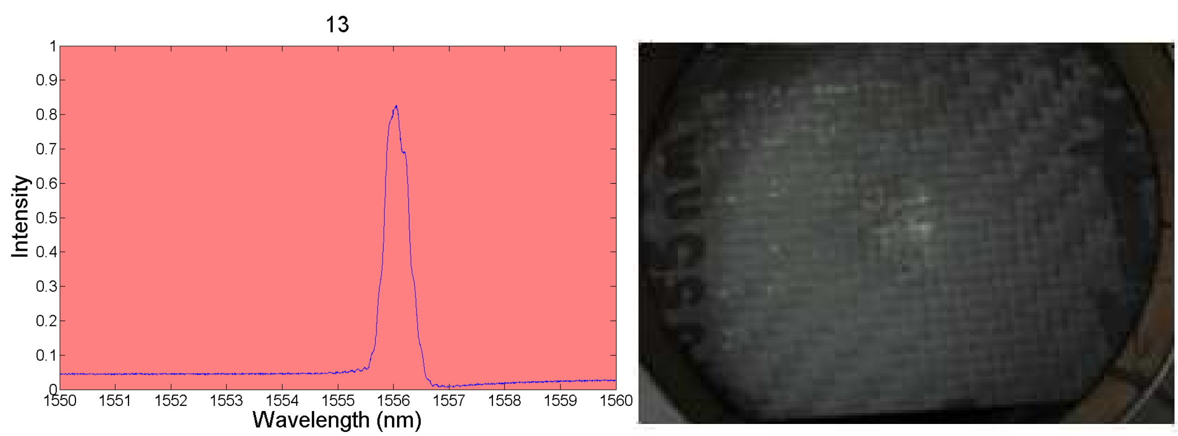

(c)

Figure 3.15. Comparison of reflected Bragg spectrum and impacted damage in specimen 24 after (a) strike 7, (b) strike 9, and (c) strike 13 in Region 1.

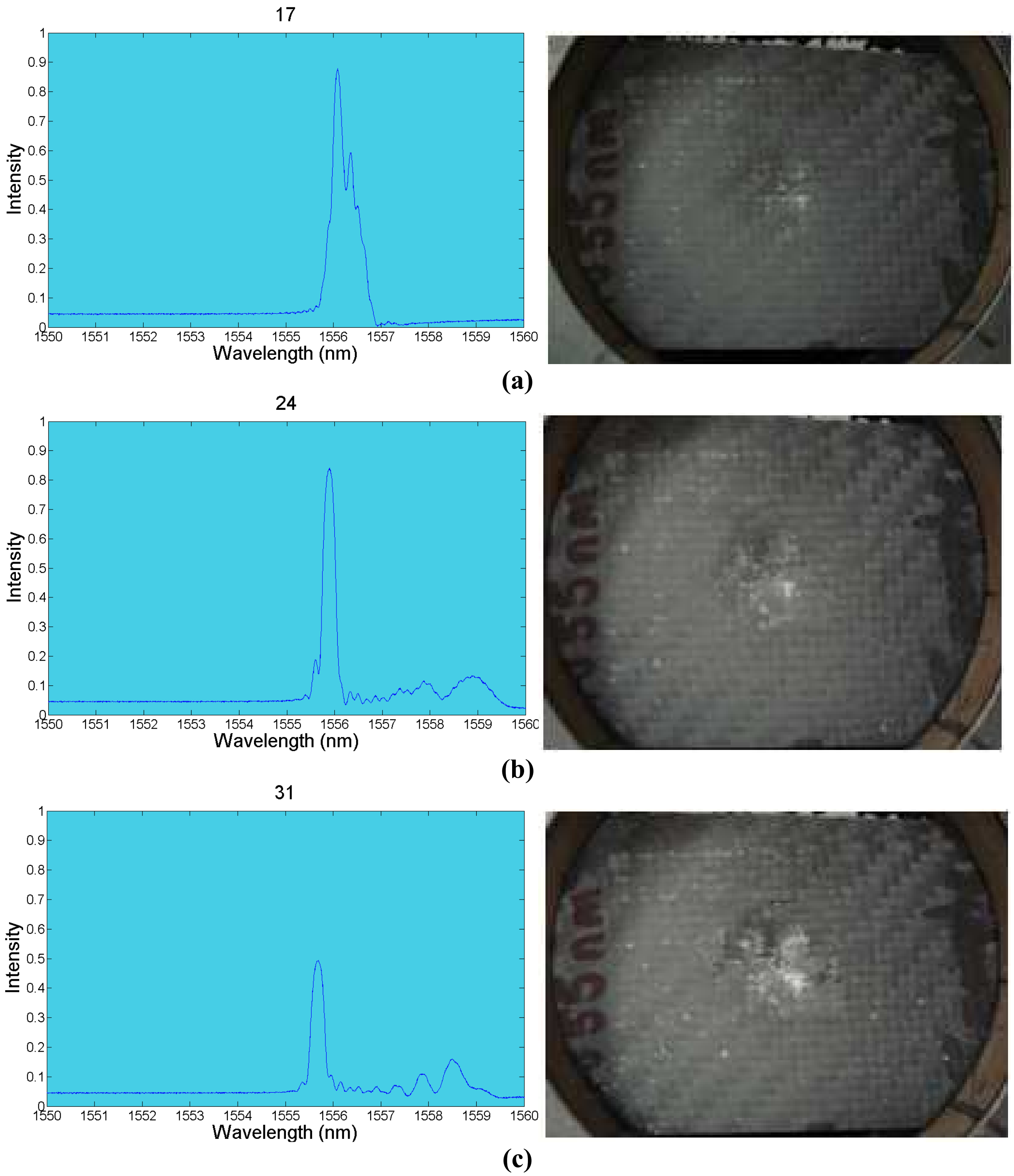

Figure 3.16. Comparison of reflected Bragg spectrum and impacted damage in specimen 24 after (a) strike 17, (b) strike 24, and (c) strike 31 in Region 2.

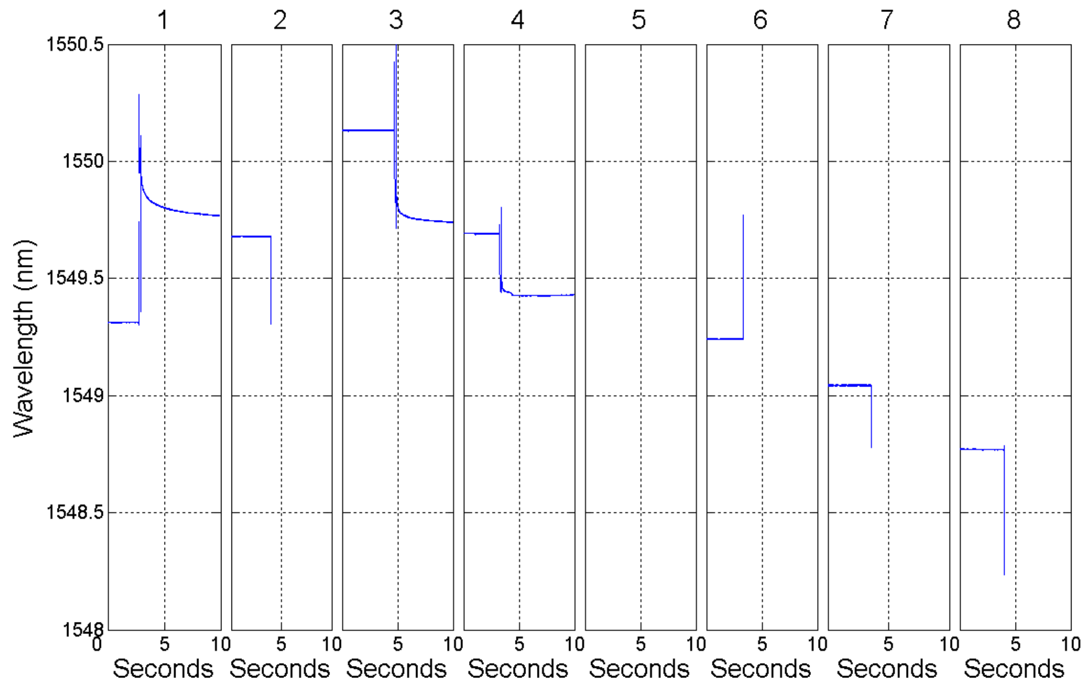

Figure 3.17. Peak wavelength change per strike of specimen 25.

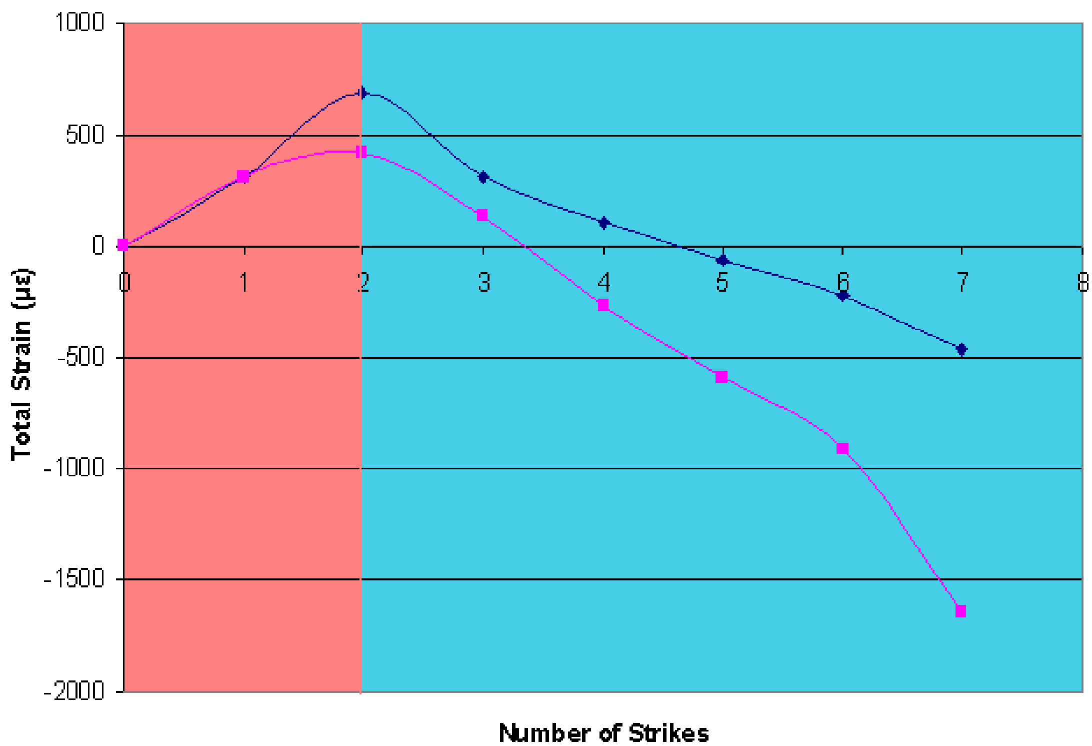

Figure 3.18. Residual strain plot for specimen 25 divided into two regions

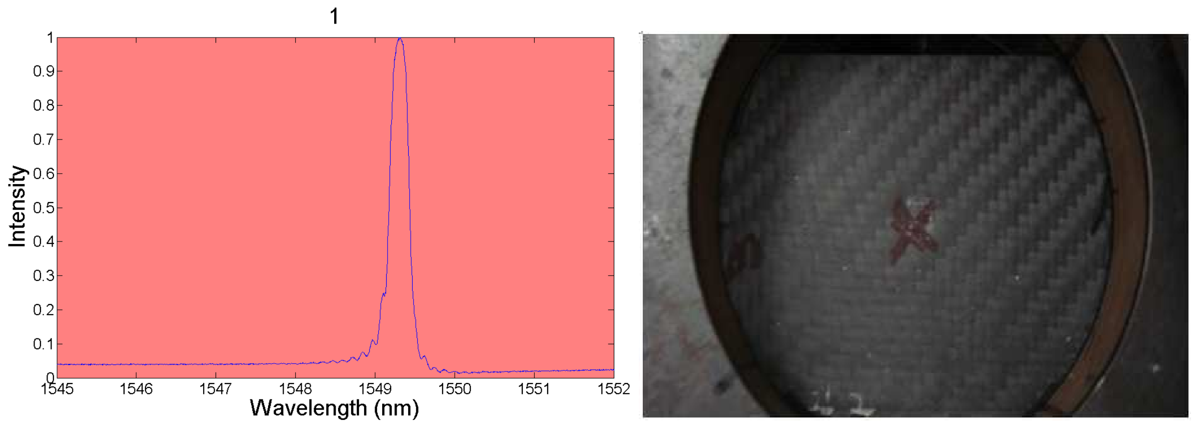

Figure 3.19. Comparison of reflected Bragg spectrum and impacted damage in specimen 25 after strike 1 in Region 1.

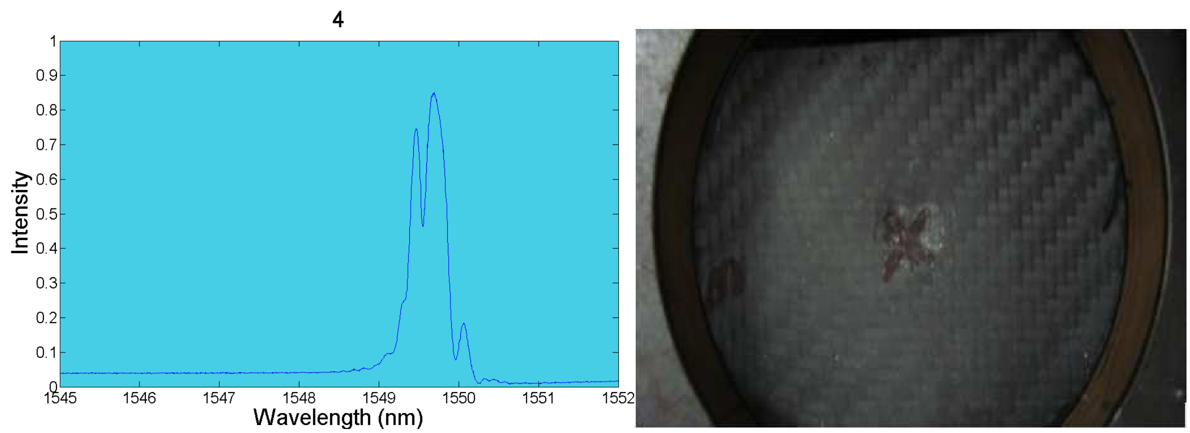

(a)

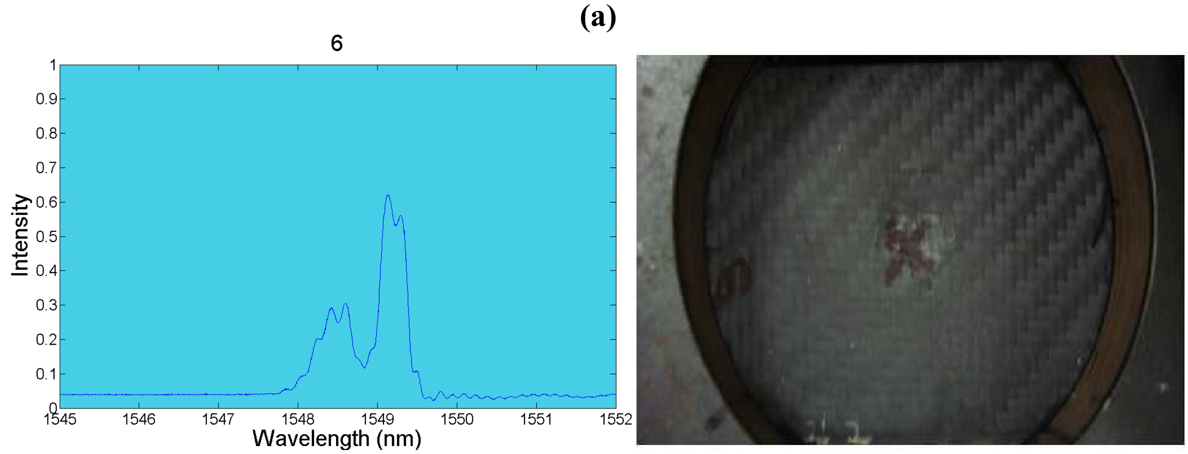

(b)

Figure 3.20. Comparison of reflected Bragg spectrum and impacted damage in specimen 25 after (a) strike 4 and (b) strike 6) in Region 2.

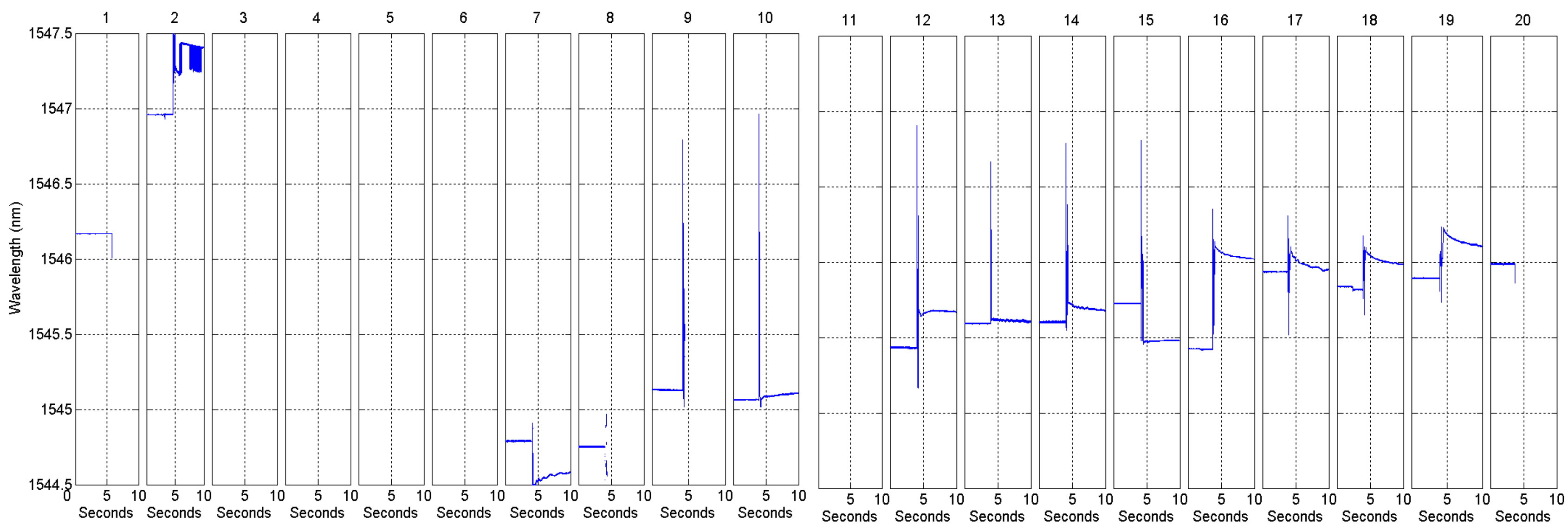

Figure 3.21. Peak wavelength change per strike of specimen 26

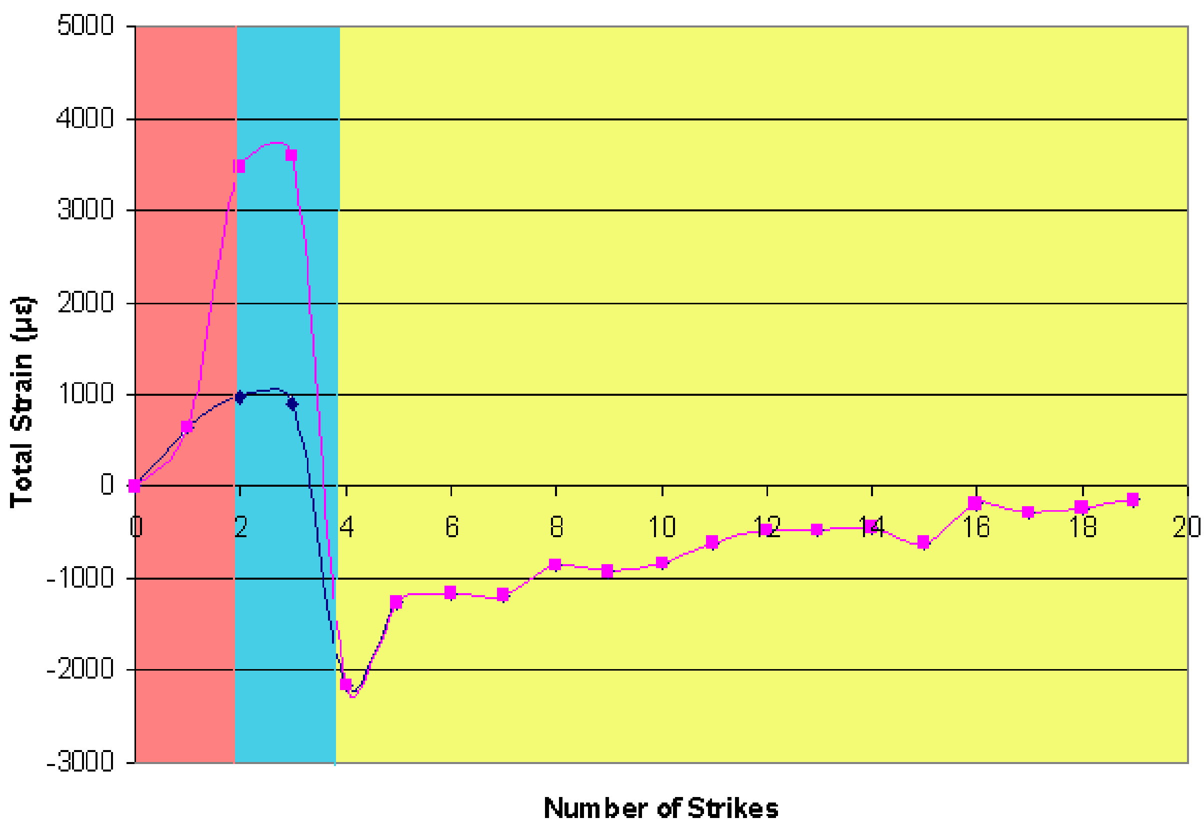

Figure 3.22. Residual strain plot for specimen 26 divided into three regions

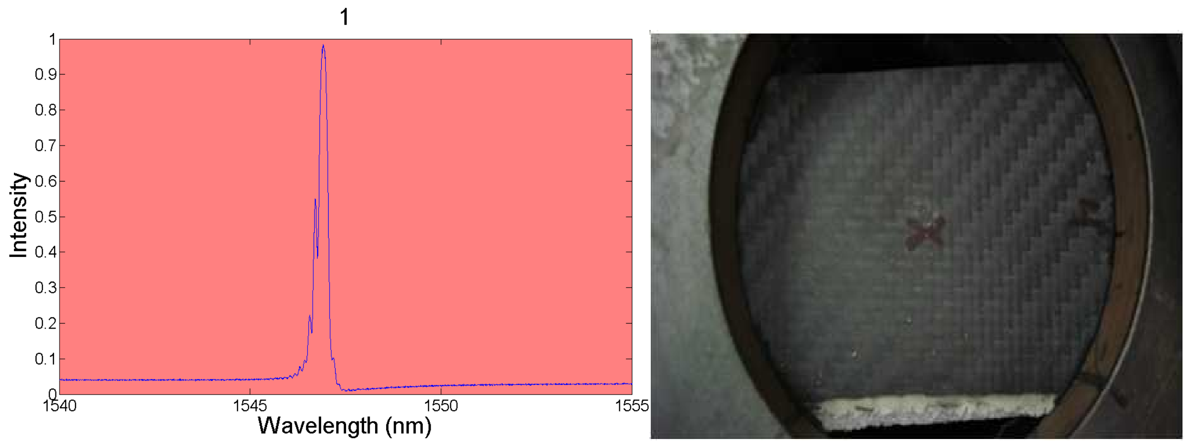

Figure 3.23. Comparison of reflected Bragg spectrum and impacted damage in specimen 26 after strike 1 in Region 1.

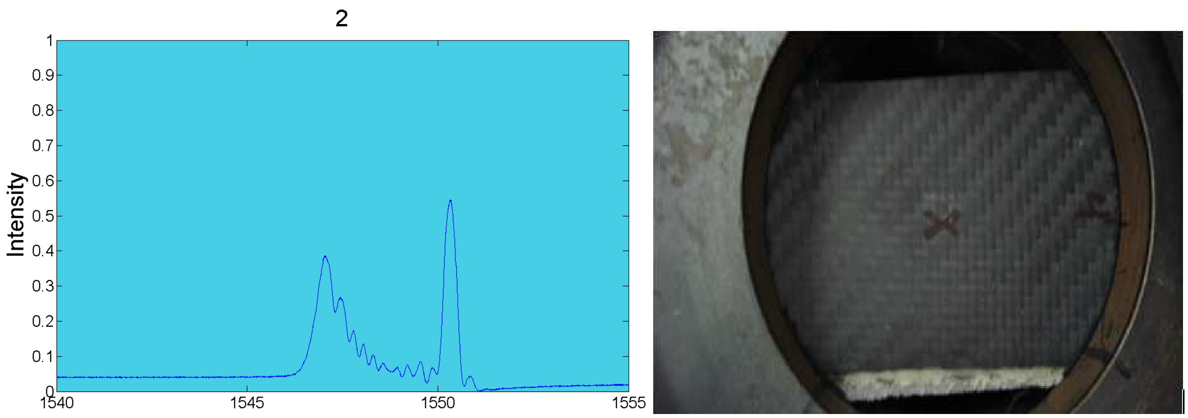

(a)

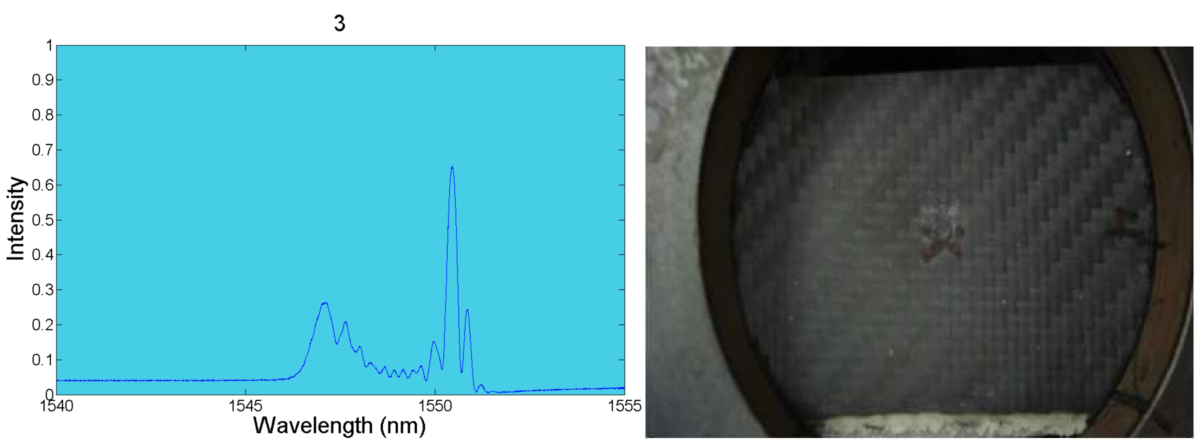

(b)

Figure 3.24. Comparison of reflected Bragg spectrum and impacted damage in specimen 26 after (a) strike 2 and (b) strike 3 in Region 2.

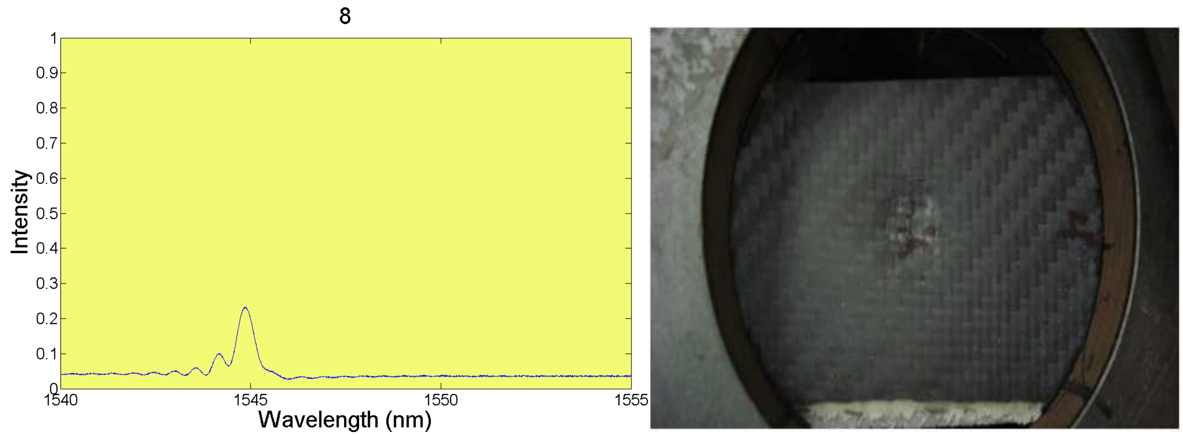

(a)

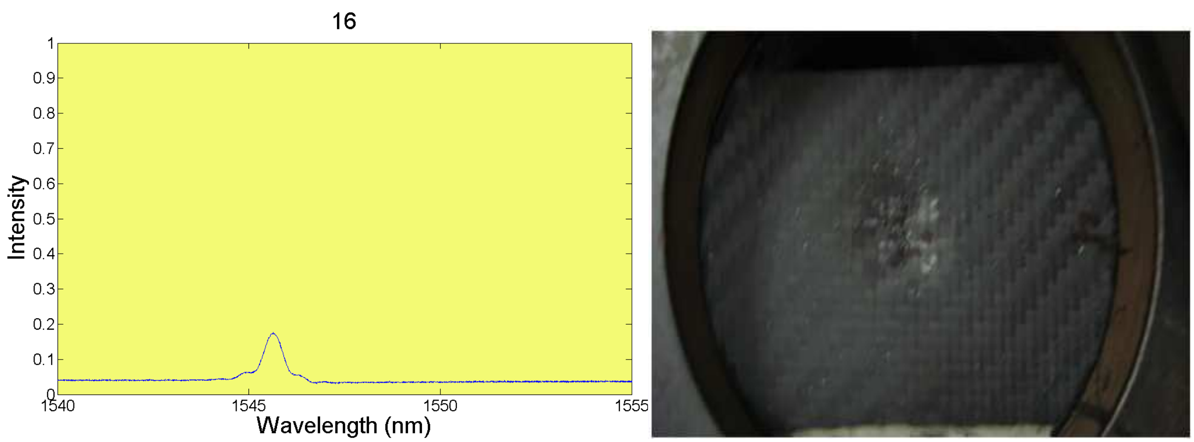

(b)

Figure 3.25. Comparison of reflected Bragg spectrum and impacted damage in specimen 26 after (a) strike 8 and (b) strike 16 in Region 3.

CHAPTER 4. CONCLUSIONS AND FUTURE WORK

Conclusions

The behavior of foam core-CFRP sandwich structures was analyzed when submitted to repeated low velocity impact strikes. There was a strong consistency between the sandwich specimens under low velocity impact. The majority of the specimens survived a similar amount of strikes when submitted to the same impact energy. Additional detail was paid to the contact force and dissipated energy response of the sandwich composites. It was determined the contact force and dissipated energy plots for each sample were similar to each other and that the maximum contact force remained fairly constant through the experimental procedure, while the specimens dissipated more energy per strike as damage in the structure increased.

Additionally, fiber Bragg grating sensors were embedded in the structure at the facesheet-core interface to measure the strain induced by low velocity impact. The FBG sensors were able to effectively detect the damage generated by each strike by both the distortion of the shape of the Bragg peak and through the wavelength shift of the peak. The wavelength shift is an axial strain on the fiber, whereas the distortion of the peak is indicative of the non-uniformity of the axial strain and transverse compression on the fiber. The peak wavelength shift measurements did not have a strong correlation to the accumulation of damage in the sandwich laminate. However, the spectral distortion did evolve throughout the initial accumulation of damage in the laminate. In all specimens, the fiber survived half the lifetime of the specimen, with the exception of one which survived over 40% of the lifetime of the specimen. It is expected that by the time a specimen is at 40% of its lifetime, impact damage is easily visible at the impact site and would easily be detected by a visual inspection.

Furthermore, any FBG sensors embedded within the structure would have detected damage by fiber failure.

Suggestions for Future Work

Further study needs to be done on the suitability of FGB sensors in CFRP-foam core sandwich composite structures for structural health monitoring. First, more specimens with embedded FBGs need to be tested. The data collected from four specimens, though enough to draw basic trends, is insufficient to create a basis for industry applications. Also, the impact of embedded optical fibers in the facesheet-core interface needs to be investigated further. Data in this study showed a decrease in the life of specimens with a single embedded optical fiber. It is not known whether that is due to experimental scatter or if the presence of a single fiber is detrimental to the integrity of the structure. How the behavior of the composite structure is affected by multiple fibers should also be analyzed with fibers running in both the longitudinal and transverse axes of the structure. Mitigation strategies for reducing the negative effects of embedded optical fibers should also be pursued.

One improvement that could be made to the experimental procedure is to use a different method to bond the facesheet to the core. The CA glue used, though it does provide a strong bond, is applied by hand and is not applied uniformly. The inconsistencies in the interface could contributing to the scatter in the impact response data.

REFERENCES

Akil Hazizan, M. and Cantwell, W.J., "The low velocity impact response of foam-based sandwich structures," Composites: Part B 33, 193-204 (2002).

Anderson, T. and Madenci, E., "Experimental investigation of low-velocity impact characteristics of sandwich composites," Composite Structures 50, 239-247 (2000).

Avrashi, J., Dancygier, O. and Ishai, O., "Damage tolerance of thick hybrid composite plate containing a local hemispherical damage," Composite Structures 33, 227-236 (1995).

Balageas, D., Bourasseau, S., Dupont, M., Bocherens, E., Dewynter-Marty, V. & Ferdinand, P., "Comparison between Non-Destructive Evaluation Techniques and Integrated Fiber Optic Health Monitoring Systems for Composite Sandwich Structures," Jounal of Intelligent Material Systems and Structures. 11, 426-437 (2000).

Bernard, M. L. and Lagace, P. A., "Impact resistance of composite sandwich plates," Journal of Reinforced Plastics and Composites 8, 432-445 (1989).

Caprino, G. and Teti, R., "Impact and post-impact behavior of foam core sandwich structures," Composite Structures 27, 47-55 (1994).

Daniel, I.M. and Ishai, O., [Engineering Mechanics of Composite Materials 2nd Ed.], Oxford University Press, New York & Oxford, 196-198 (2006).

Freeman, B., Schwingler, E., Mahinfalah, M. and Kellog, K., "The effect of low-velocity impact on the fatigue life of sandwich composites," Composite Structures 70, 374-381 (2005).

Garrett, R., Peters, K. and Zikry, M. A. 2009. "In-situ Impact-induced Damage Assessment of Woven Composite Laminates through a Fiber Bragg Grating Sensors Network," *Journal of the Royal Aeronautical Society* , 113: 357-370.

Hosur, M.V., Mohammed, A.A., Zainuddin, S. & Jeelani, S., "Impact performance of nanophased foam core sandwich composites," Materials Science & Engineering 489, 100-109 (2008).

Koissin, V. & Shipsha, A., "Residual dent in locally loaded foam core sandwich structures - analysis and use for NDI," Composites Science and Technology 68, 57-74 (2008).

Lee J.L., Huang, K.Y. & Fann Y.J., "Dynamic Responses of Composite Sandwich Plate Impacted by a Rigid Ball," Journal of Composite Materials 27, 1238-1256 (1998).

Lee, L. J., Huang, K. Y. and Fann, Y. J., "Dynamic response of composite sandwich plate impacted by a rigid ball," Journal of Composite Materials 27, 1238-1256 (1993).

Leijten, J., Bersee, H. E. N., Bergsma O. K. and Beukers, A., "Experimental study of the low-velocity impact behaviour of primary sandwich structures in aircraft," Composites Part A 40, 164-175 (2009).

Lim, T.S., Lee, C.S. & Lee, D.G., “Failure modes of foam core sandwich beams under static and impact loads,” Journal of Composite Materials 38, 1639-1662 (2004).

Maldague, X. P. V., Theory and practice of infrared technology for nondestructive testing, John Wiley & Sons, New York, NY (2001).

Minakuchi, S., Okabe, Y., Mizutani, T. and Takeda, N., " Barely visible impact damage detection in composite sandwich structures by optical-fiber-based distributed strain measurement," Smart Materials and Structures 18, 085018 (2009）.

Minakuchi, S., Okabe, Y. & Takeda, N., “Real-time Detection of Debonding between Honeycomb Core and Facesheet using a Small-diameter FBG Sensor Embedded in Adhesive Layer,” Journal of Sandwich Structures and Materials, 9-33 (2007).

Nemes, J. A. and Simmonds, K. E., "Low-velocity impact response of foam-core sandwich composites," Journal of Composite Materials 26, 500-519 (1992)

Pearson, J. D., Zikry, M. A., Prabhugoud, M. and Peters K. 2007. “Global-local Assessment of Low-velocity Impact Damage in Woven Composites,” *Journal of Composite Materials,* 41:2759-2783.

Propst, A., Peters, K., Zikry, M.A., Schultz, S., Kunzler, W., Zhu, Z., Wirthlin, M. and Selfridge, R. 2010. “Assessment of Damage in Composite Laminates through Dynamic, Full-spectral Interrogation of Fiber Bragg Grating Sensors,” *Smart Materials and Structures*, 19: 015016.

Schubel, P.M., Lou, J.-J. & Daniel, I.M., “Impact and post impact behavior of composite sandwich panels,” Composites: Part A 38, 1051-1057 (2007).

Shipsha, A. & Zenkert, D., “Compression-after-impact strength of sandwich panels with core crushing damage,” Applied Composite Materials 12, 149-164 (2005).

Shipsha, A., Hallström, S. & Zenkert, D., “Failure mechanisms and modeling of impact damage in sandwich beams – a 2D approach: part 1 – experimental investigation,” Journal of Sandwich Structures and Materials 5, 7-31 (2003).

Torre, L. & Kenny, J.M., “Impact testing and simulation of composite sandwich structures for civil transportation,” Composite Structures 50, 257-267 (2000).

Vaidya, U.K., Nelson, S., Sinn, B. & Mathew, B., “Processing and high strain rate impact response of multi-functional sandwich composites,” Composite Structures 52, 429-440 (2001).

Wu, C.L. & Sun, C.T., “Low velocity impact damage in composite sandwich beams,” Composite Structures 34, 21-27 (1996).

APPENDIX

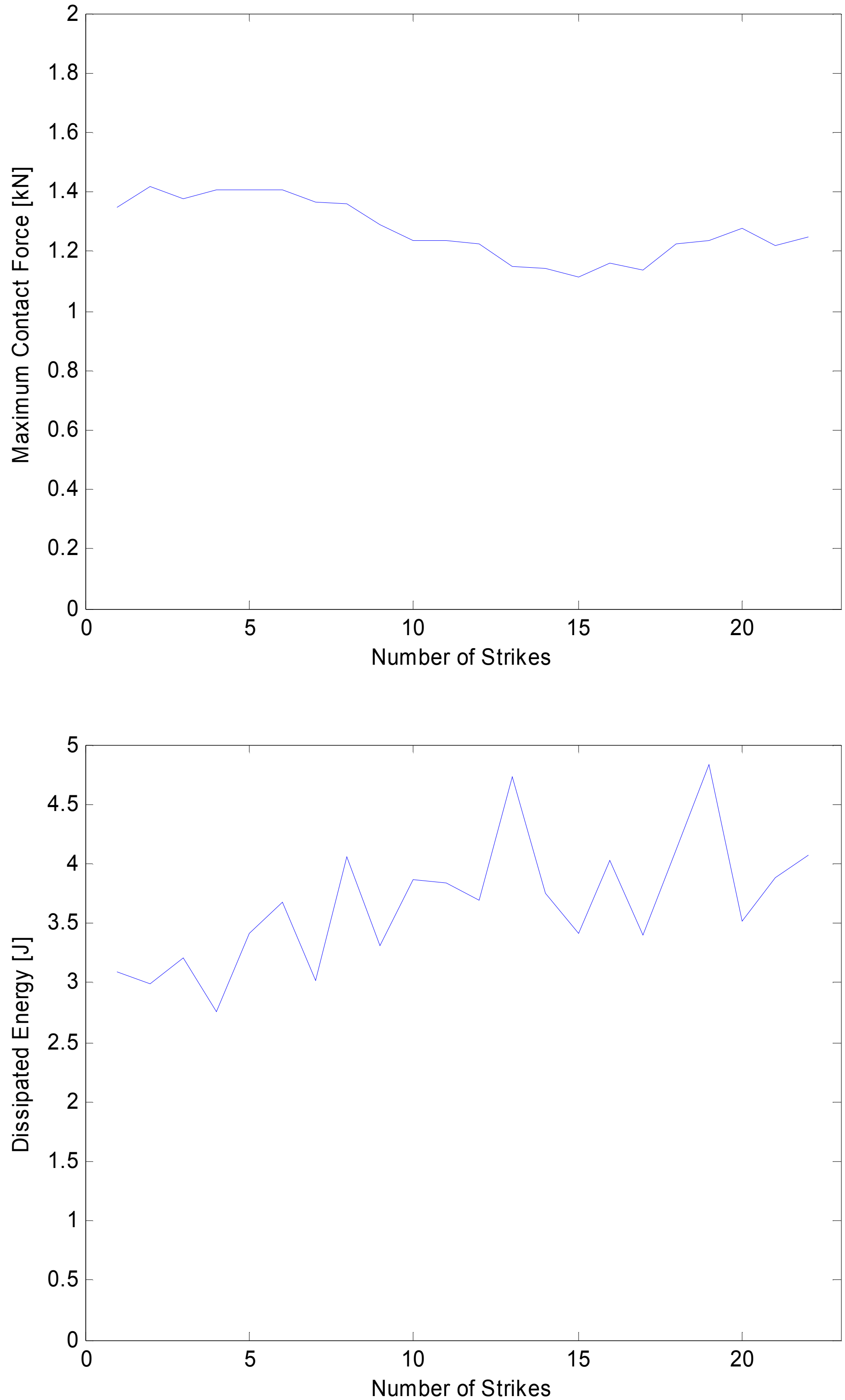

Figure A.1. Maximum contact force and dissipated energy plots for specimen 2.

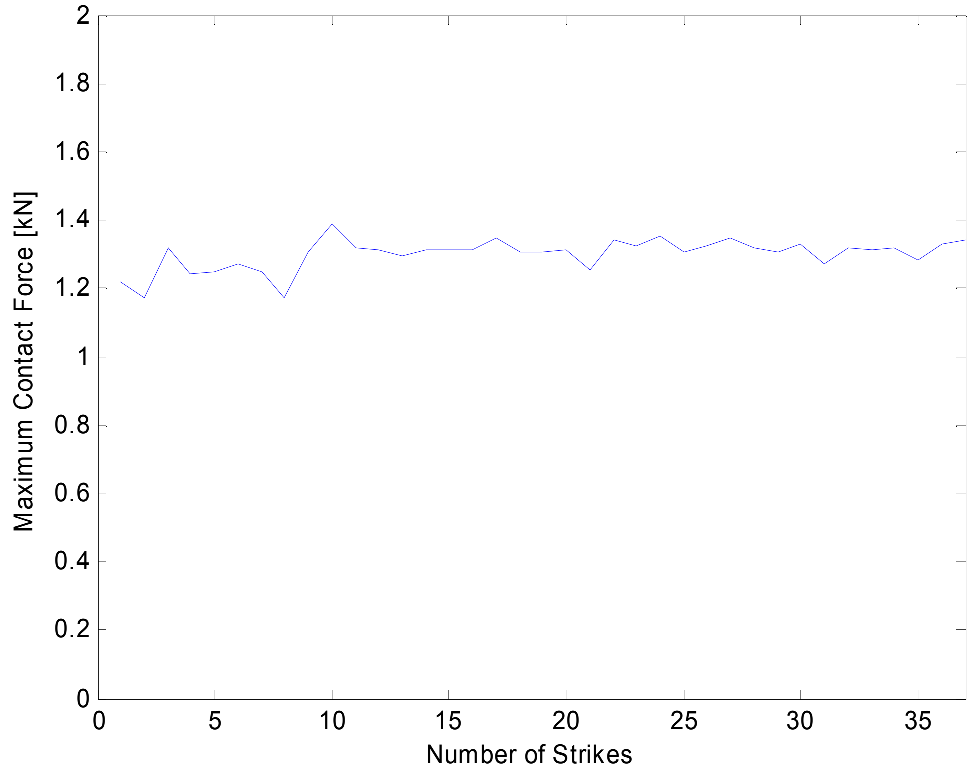

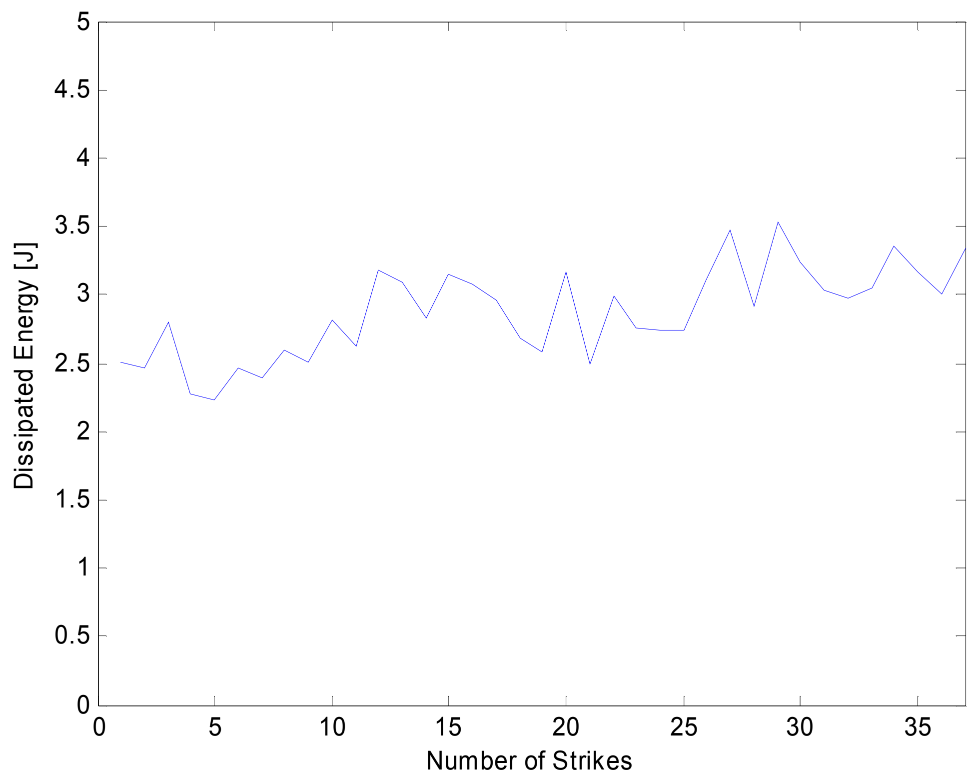

Figure A.2. Maximum contact force and dissipated energy plots for specimen 3.

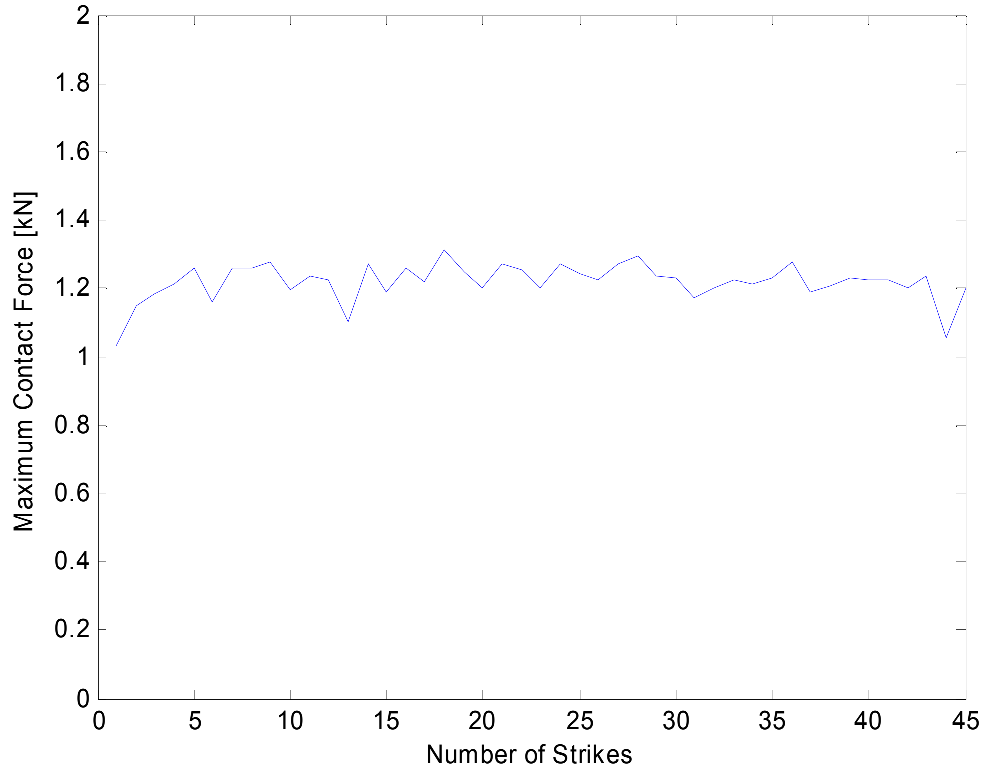

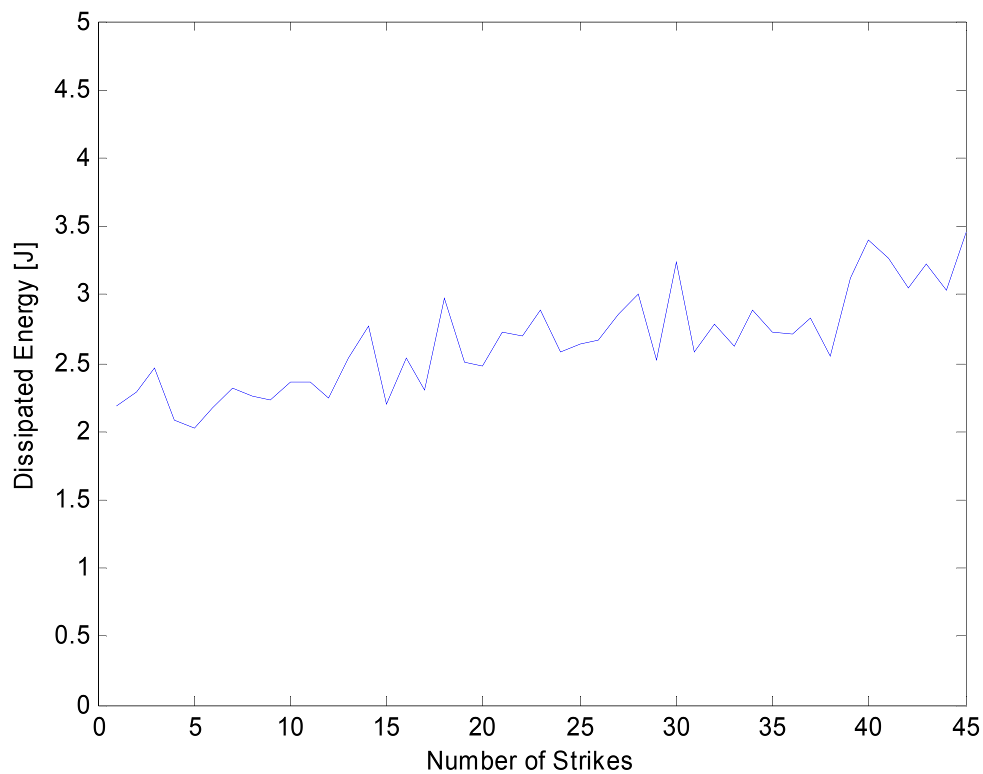

Figure A.3. Maximum contact force and dissipated energy plots for specimen 4.

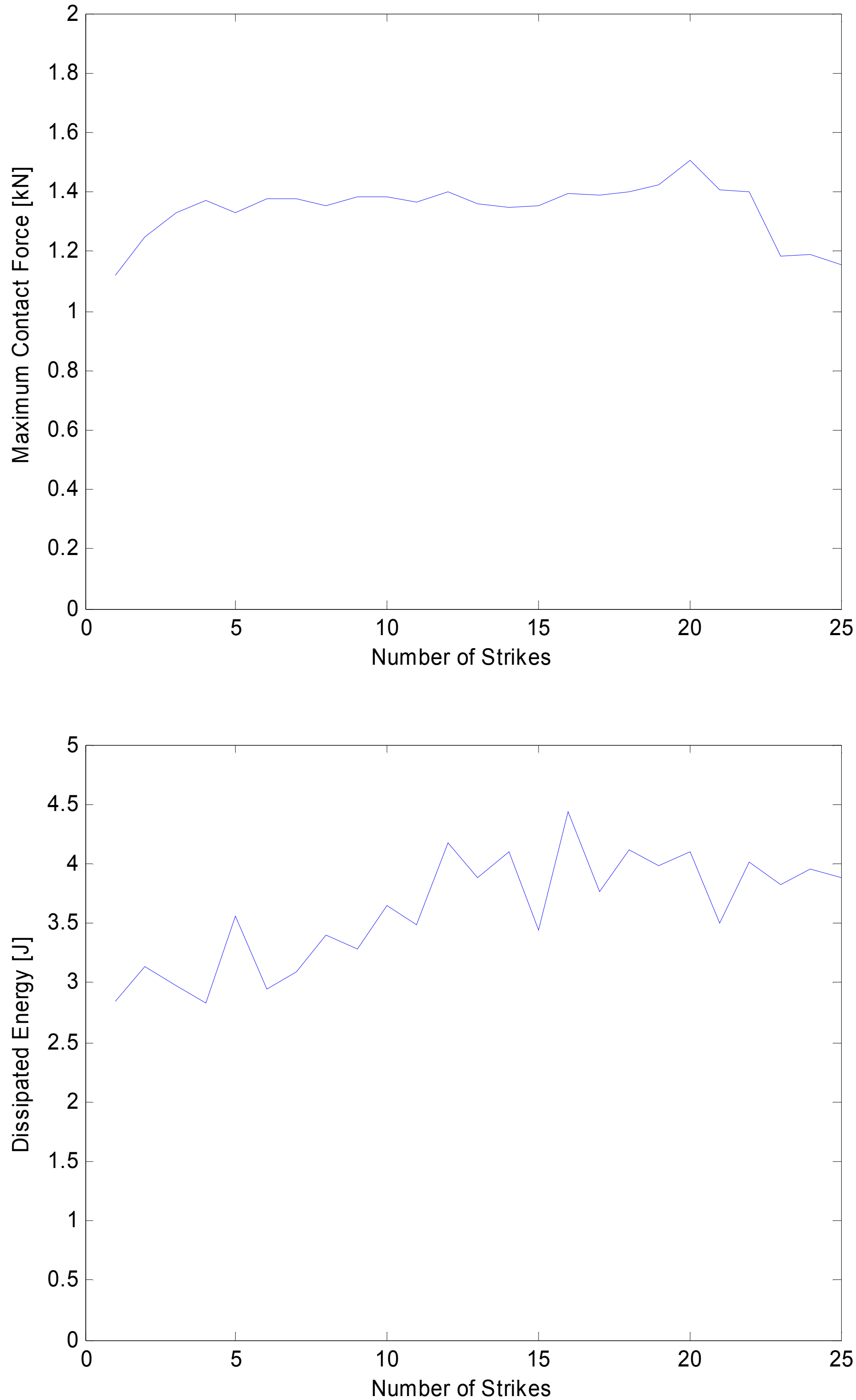

Figure A.4. Maximum contact force and dissipated energy plots for specimen 5.

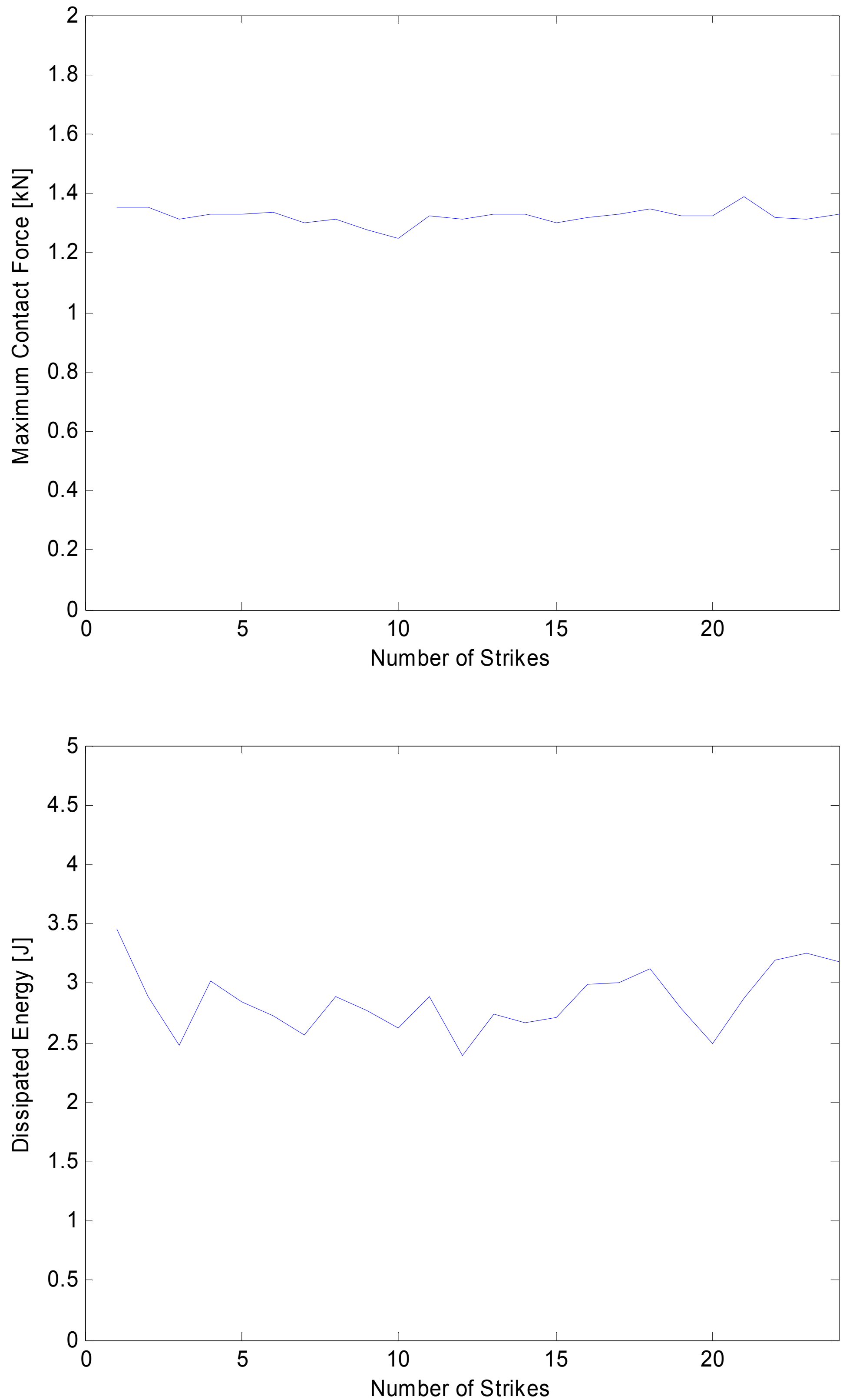

Figure A.5. Maximum contact force and dissipated energy plots for specimen 6.

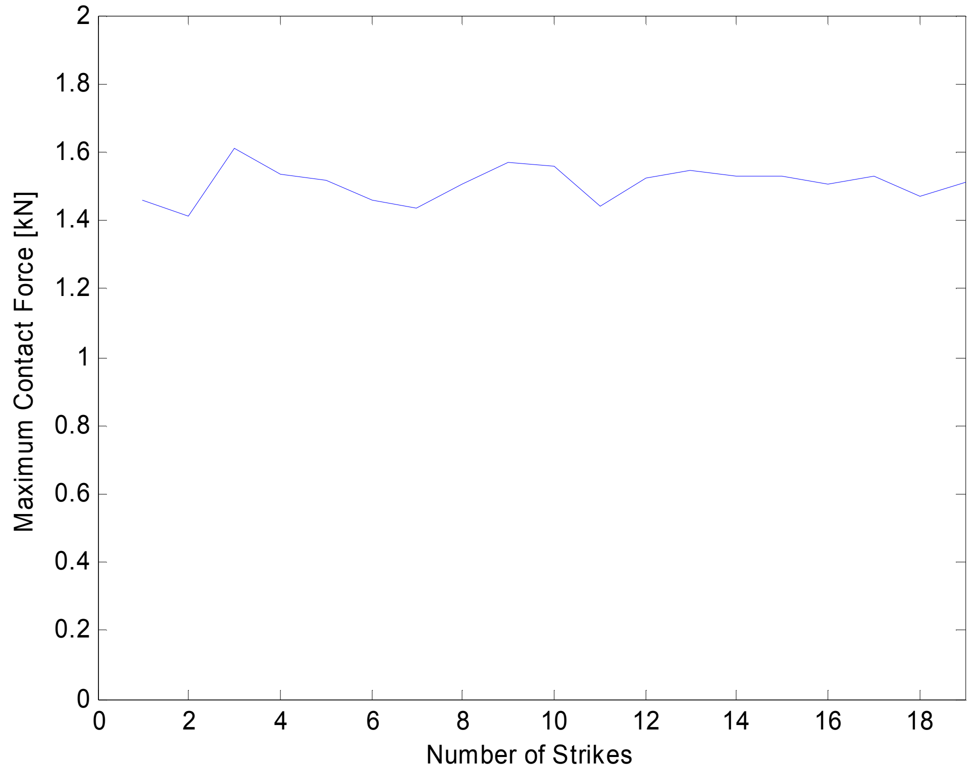

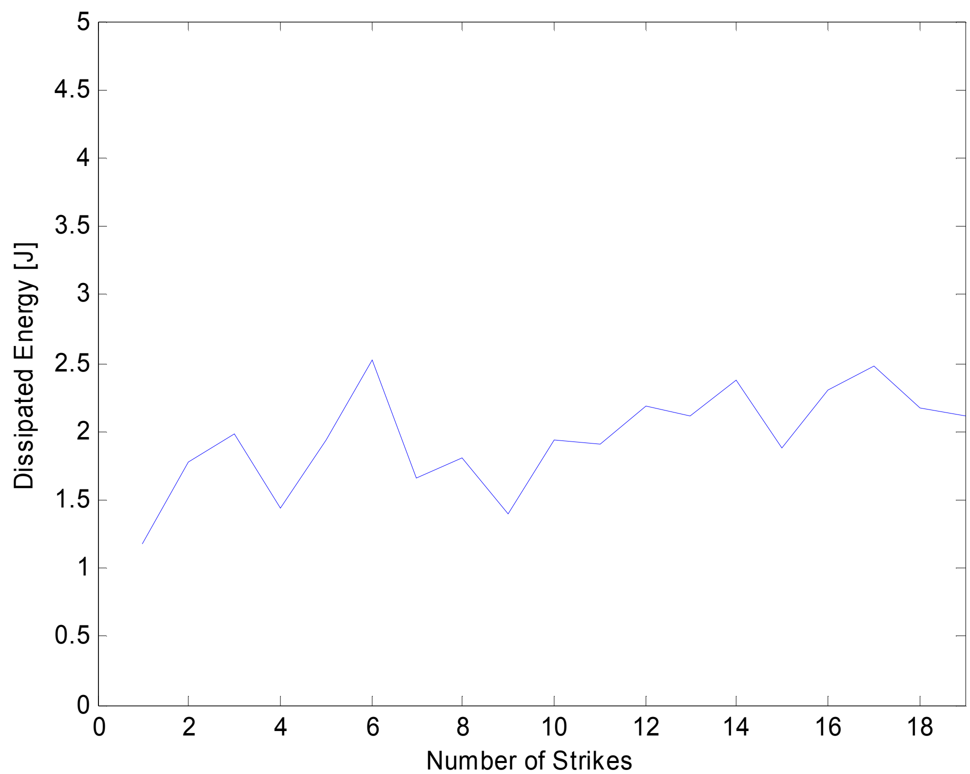

Figure A.6. Maximum contact force and dissipated energy plots for specimen 7.

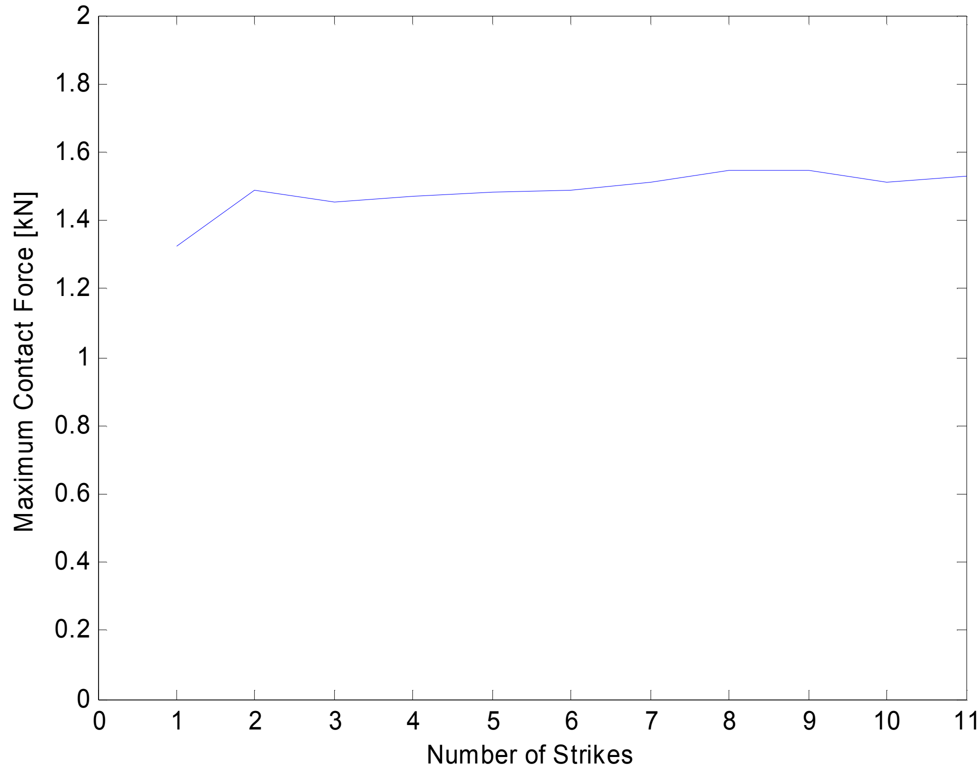

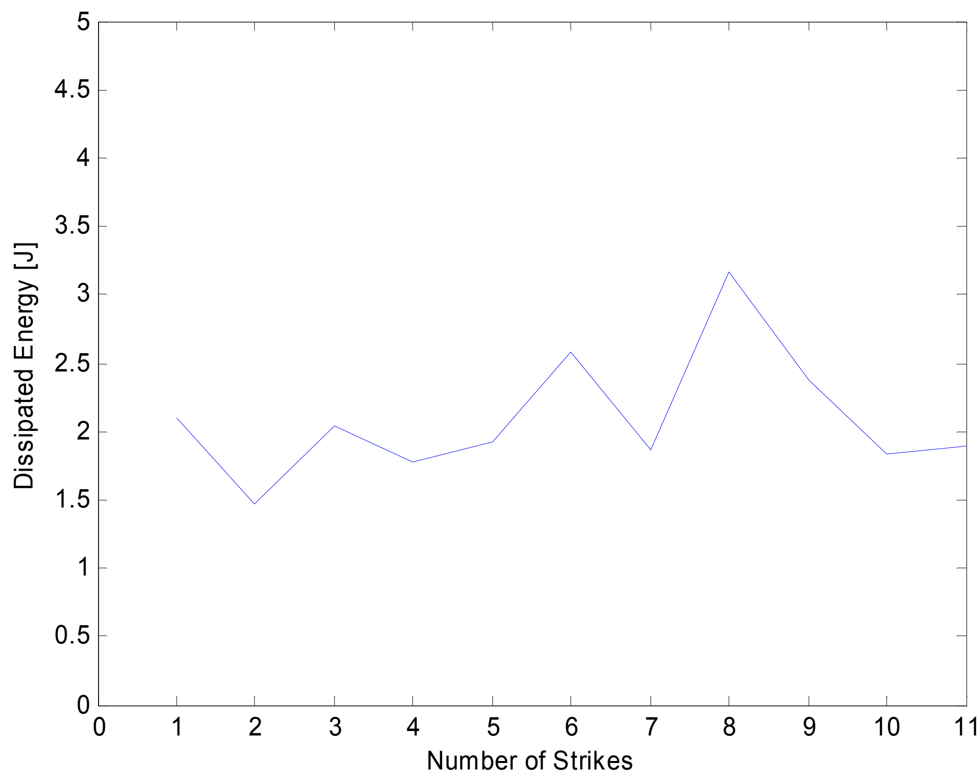

Figure A.7. Maximum contact force and dissipated energy plots for specimen 8.

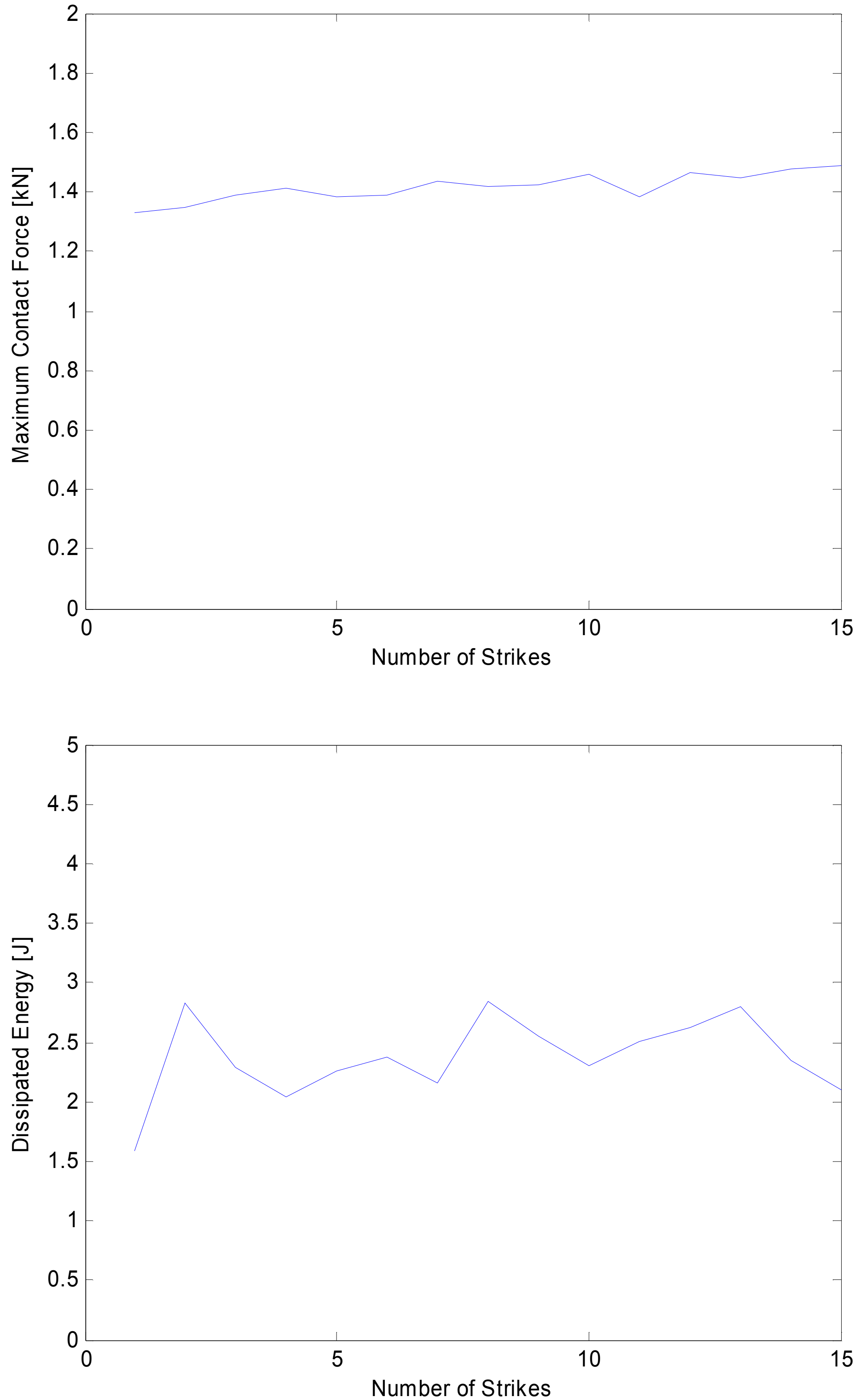

Figure A.8. Maximum contact force and dissipated energy plots for specimen 9.

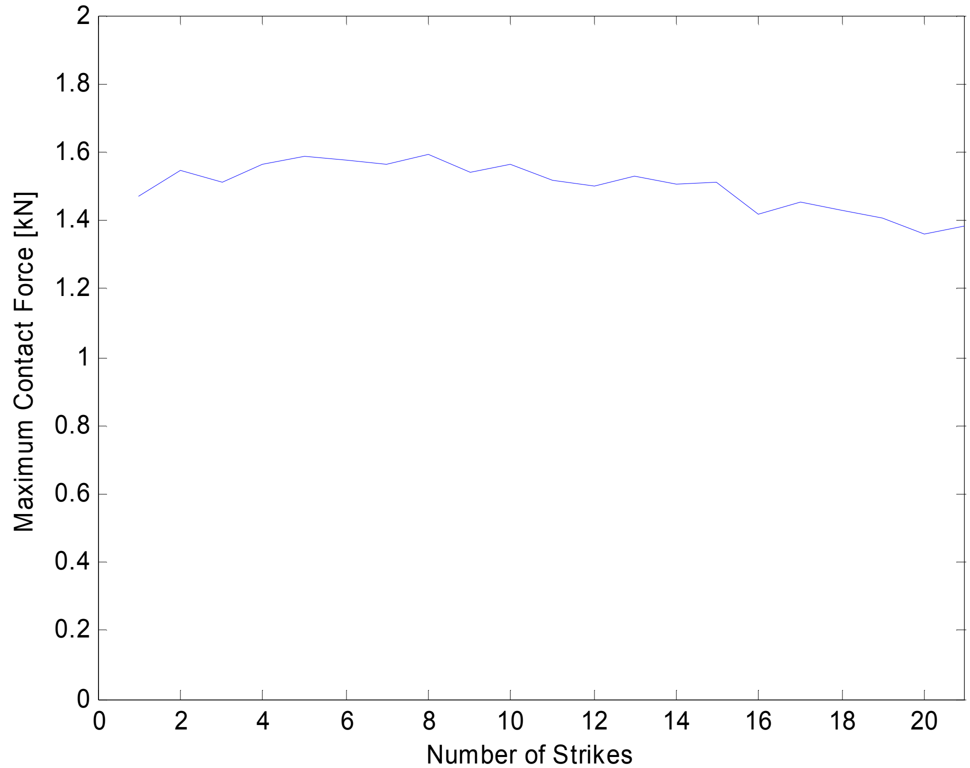

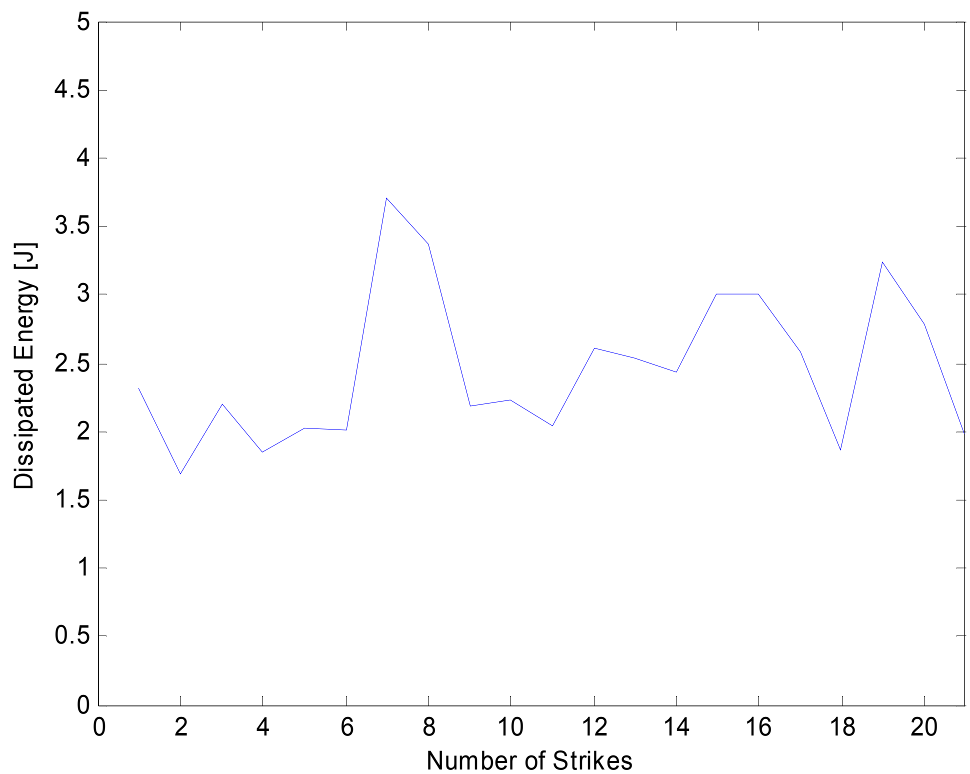

Figure A.9. Maximum contact force and dissipated energy plots for specimen 10.

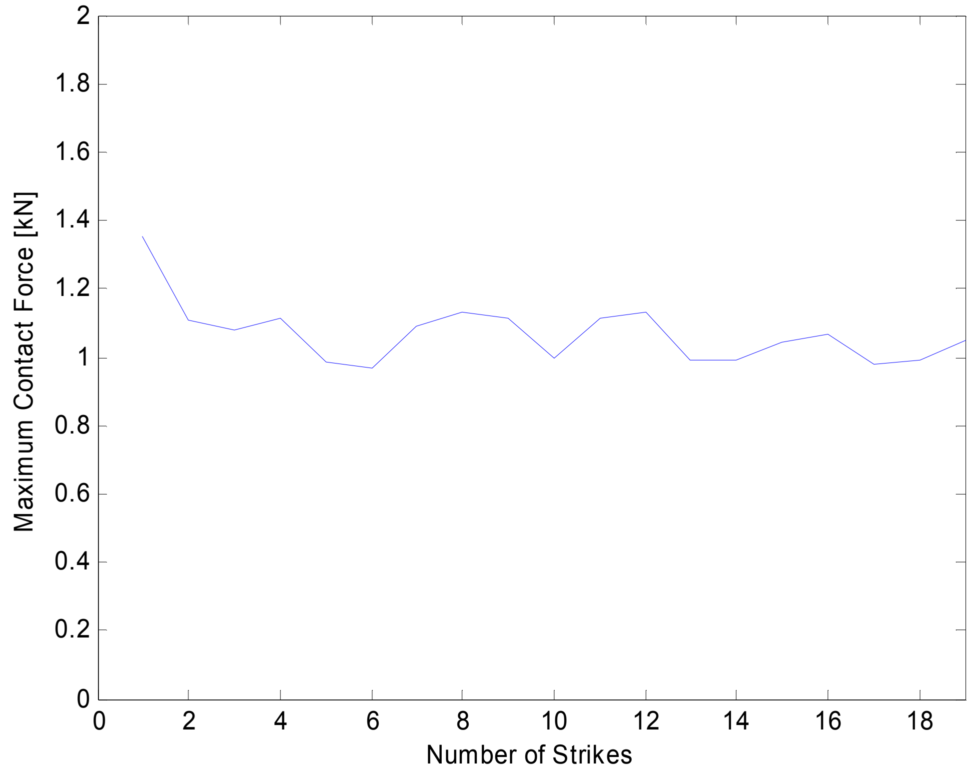

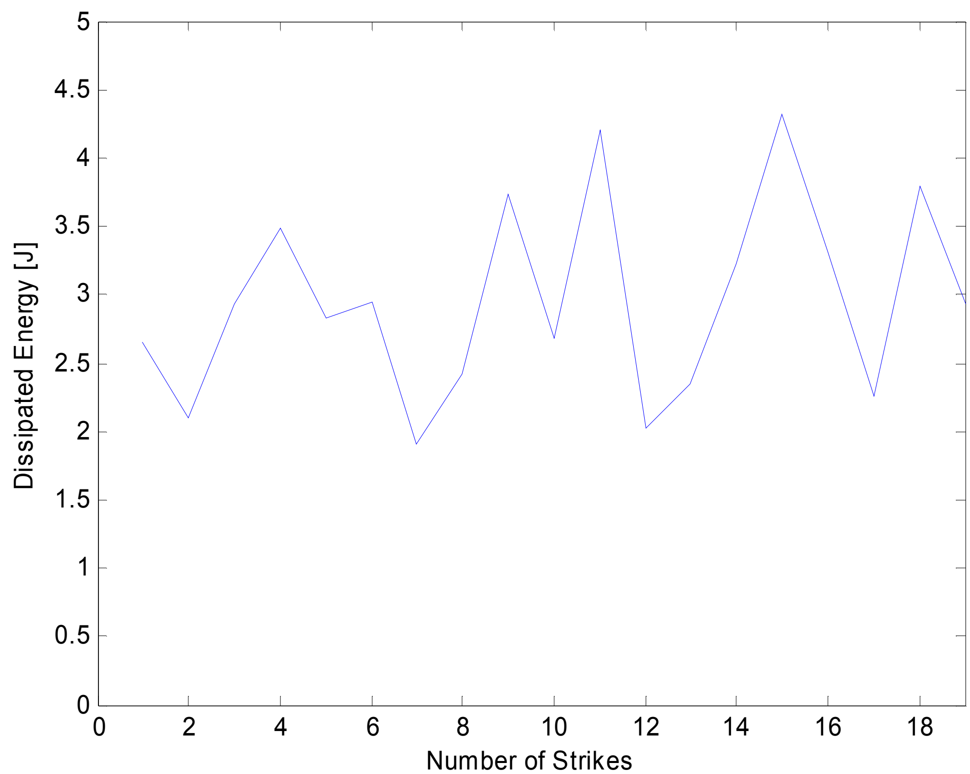

Figure A.10. Maximum contact force and dissipated energy plots for specimen 11.

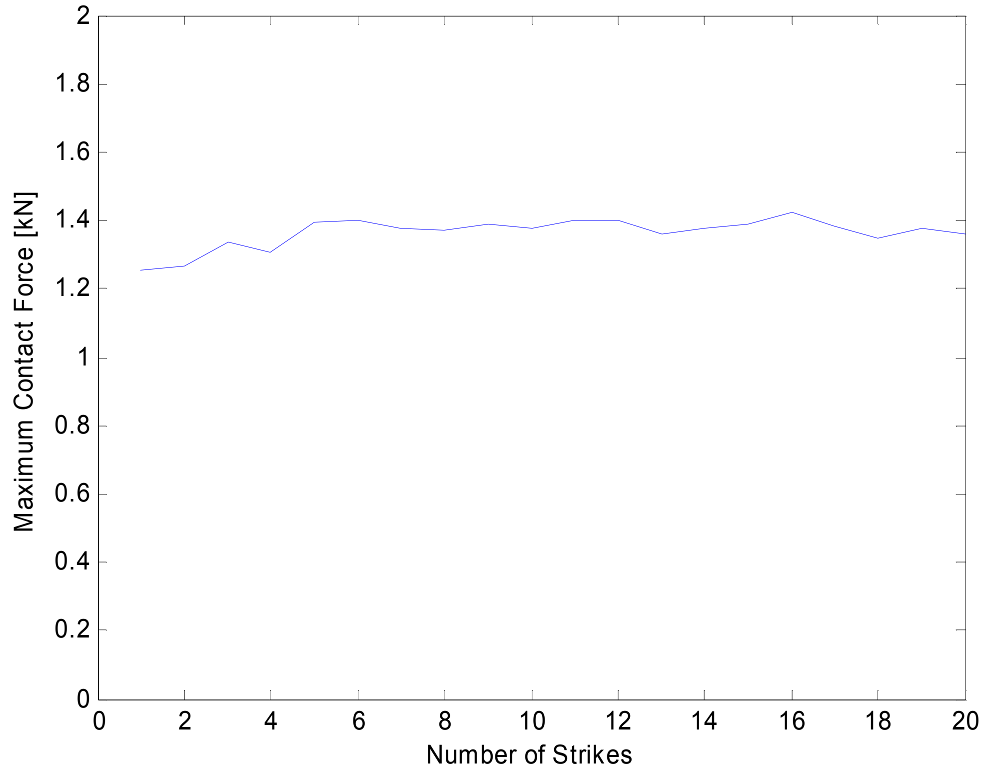

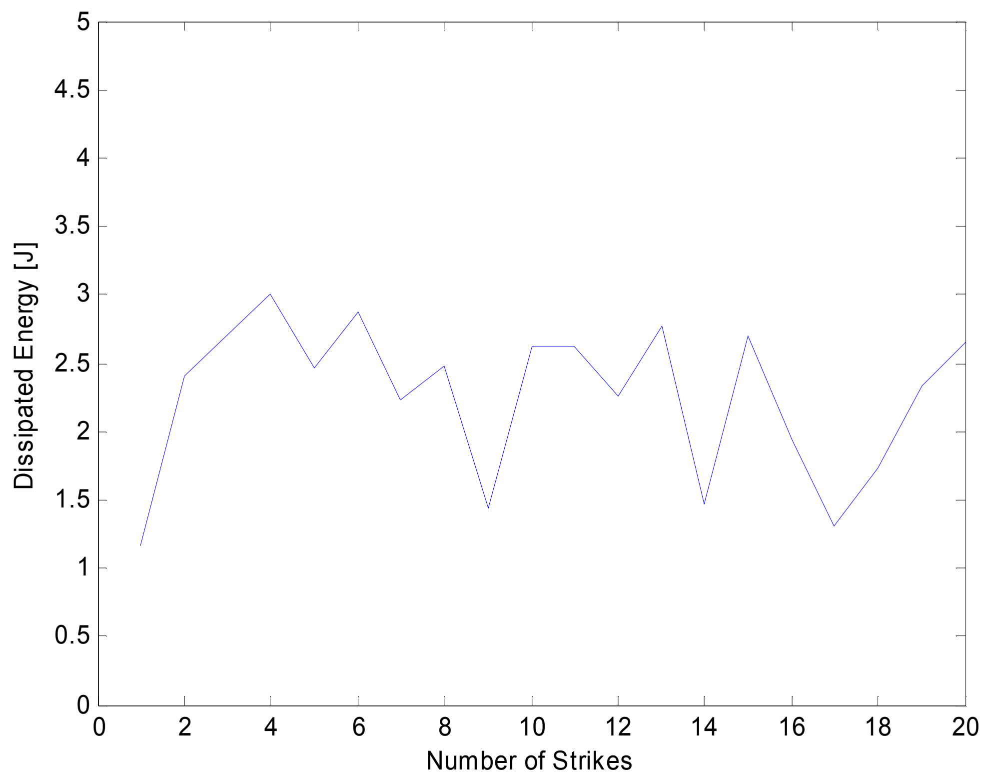

Figure A.11. Maximum contact force and dissipated energy plots for specimen 12.

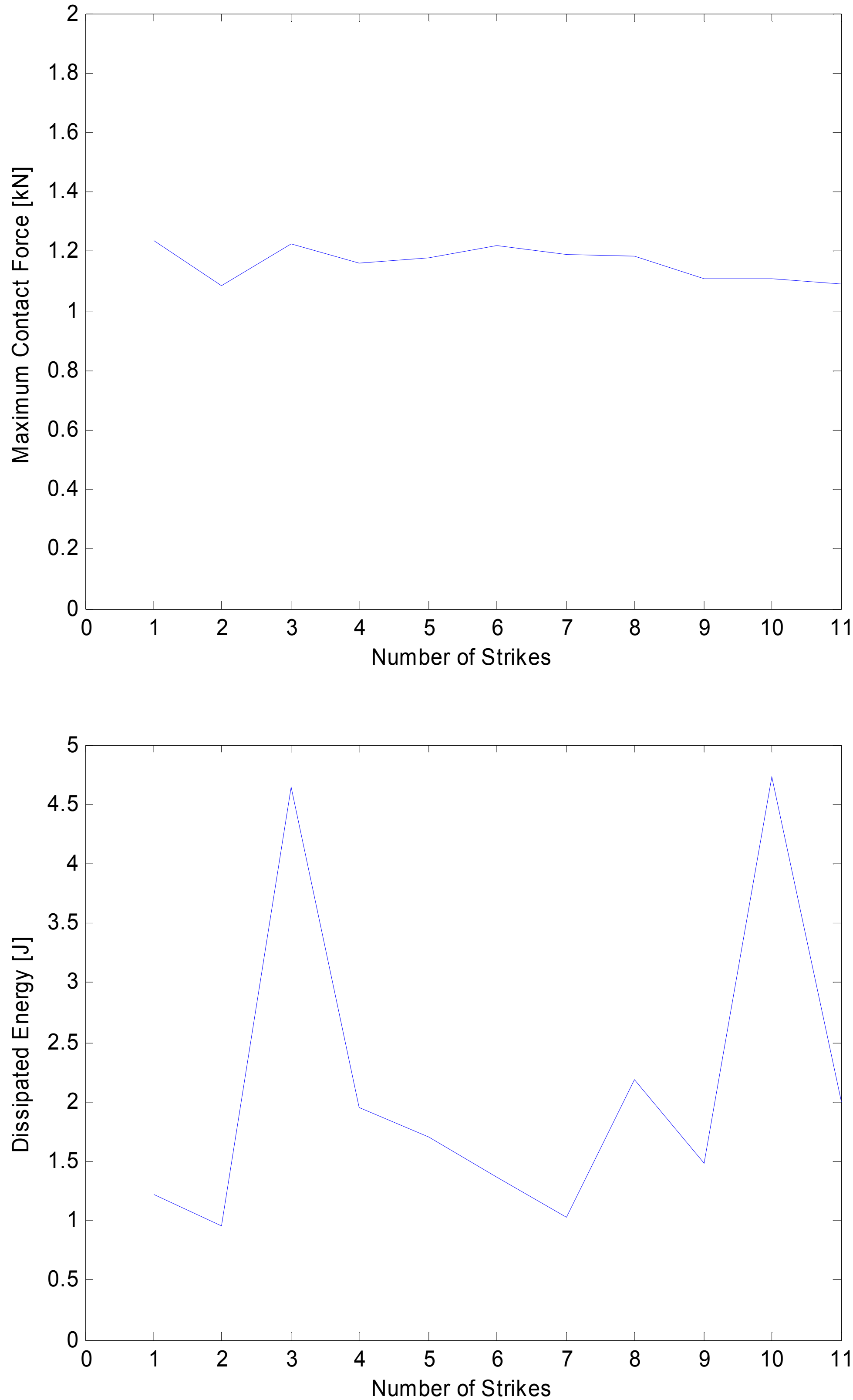

Figure A.12. Maximum contact force and dissipated energy plots for specimen 13.

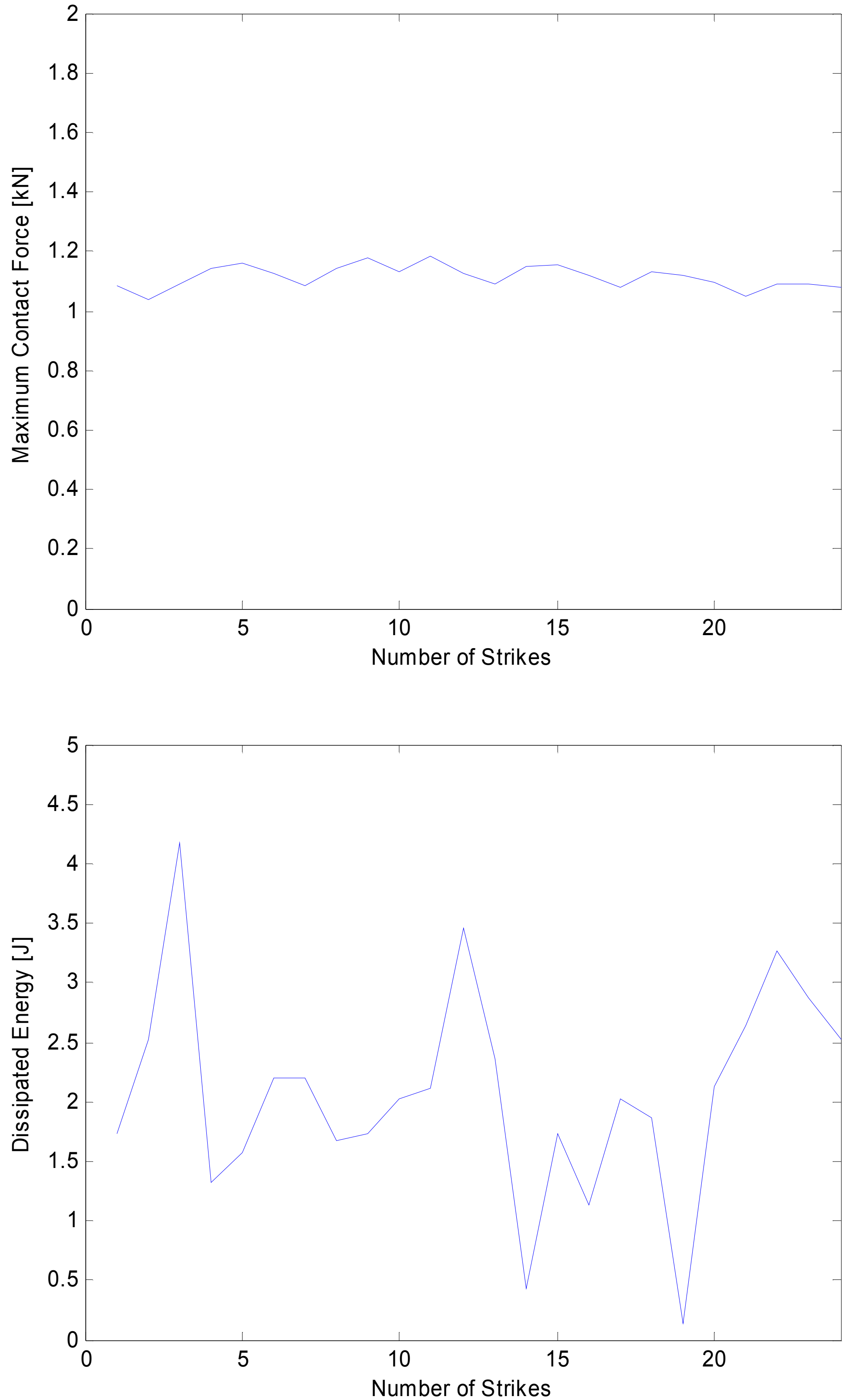

Figure A.13. Maximum contact force and dissipated energy plots for specimen 14.

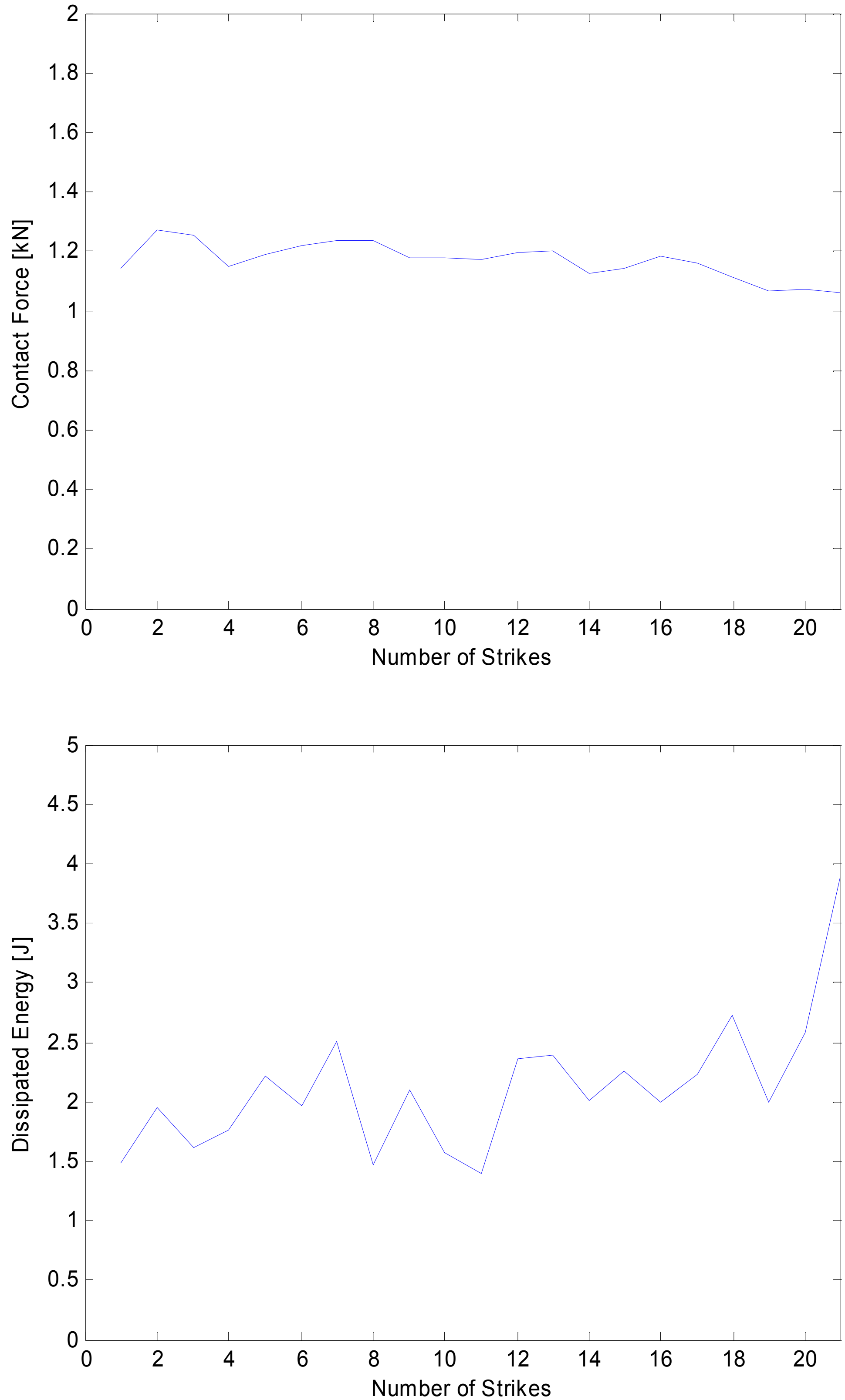

Figure A.14. Maximum contact force and dissipated energy plots for specimen 16.

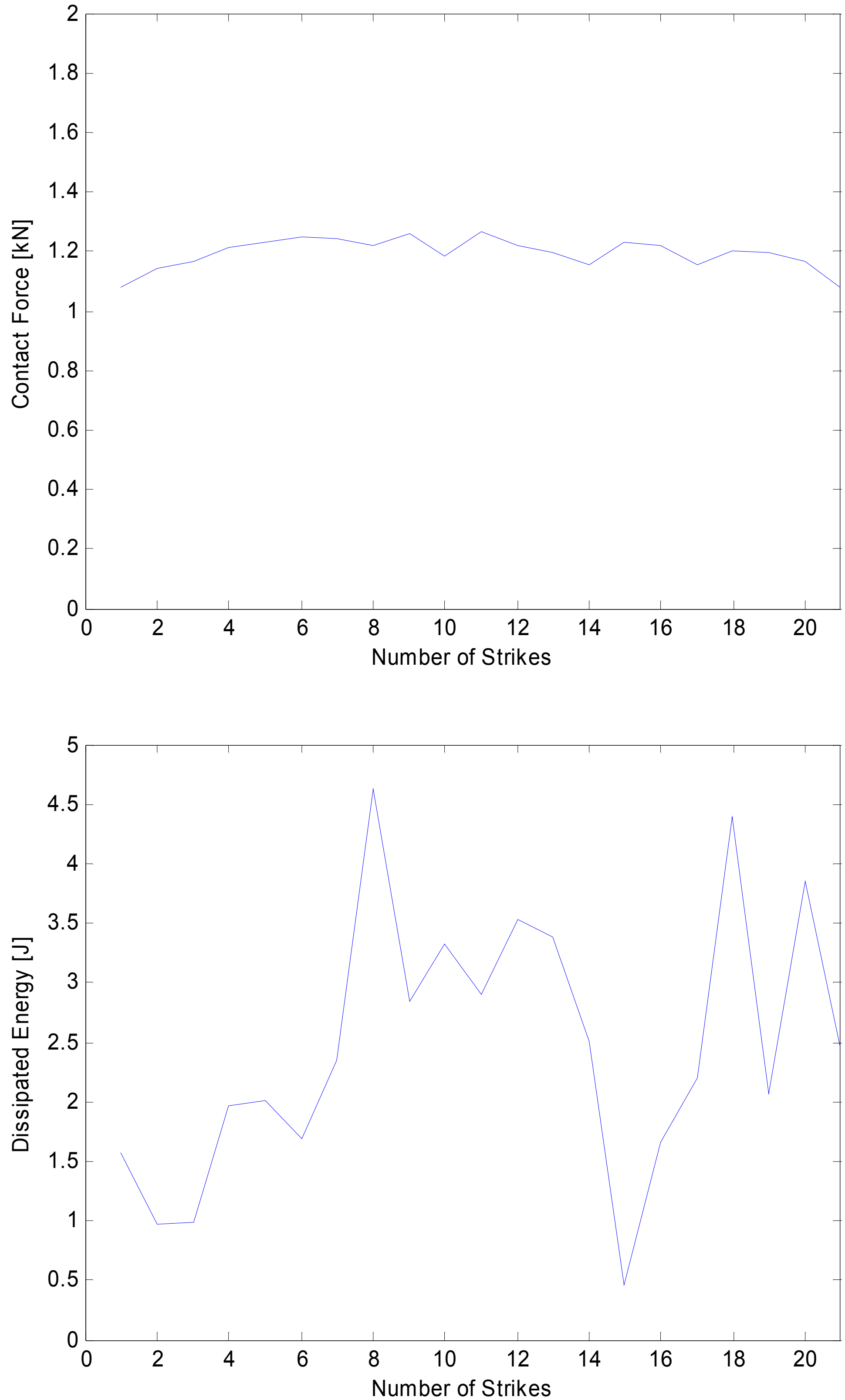

Figure A.15. Maximum contact force and dissipated energy plots for specimen 17.

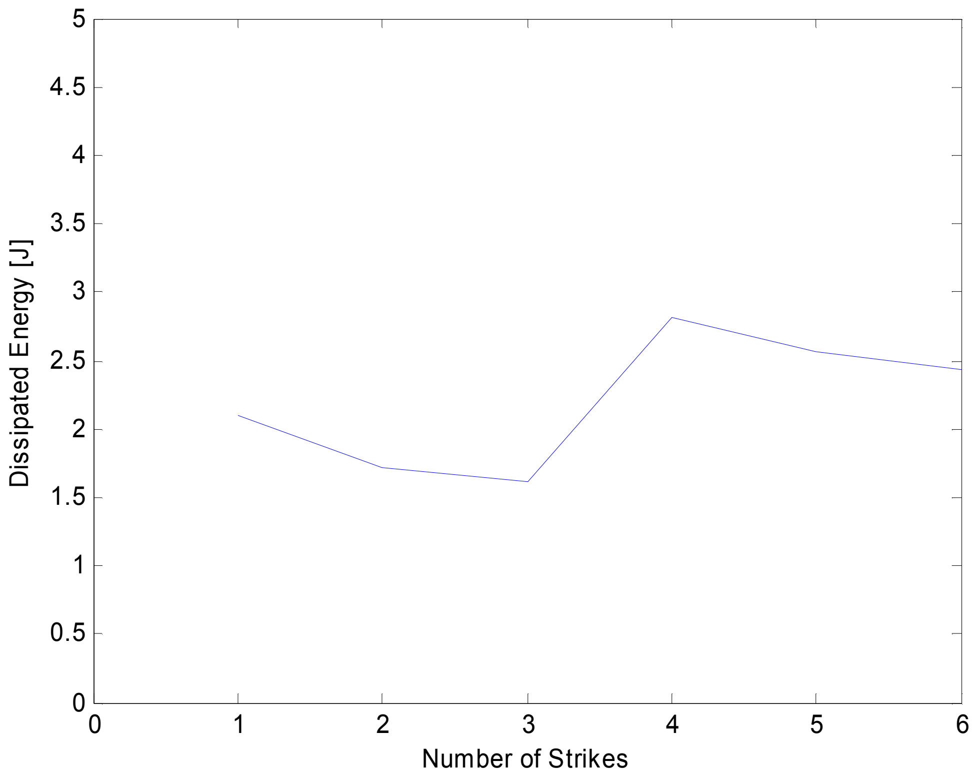

Figure A.16. Dissipated energy plot for specimen 18.

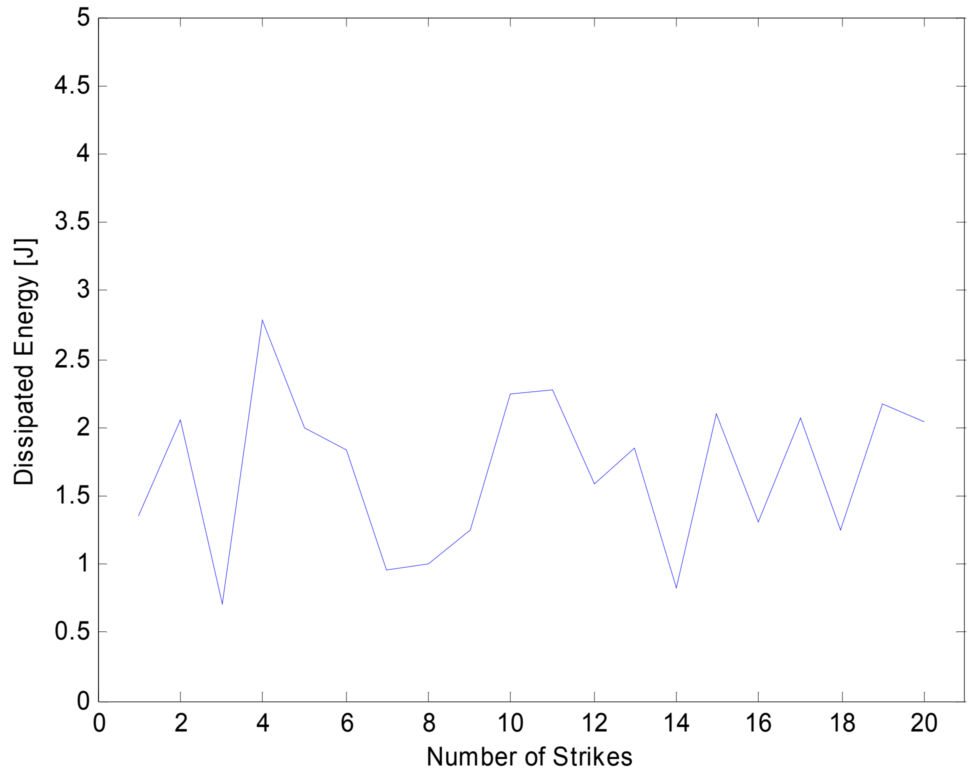

Figure A.17. Dissipated energy plot for specimen 19.

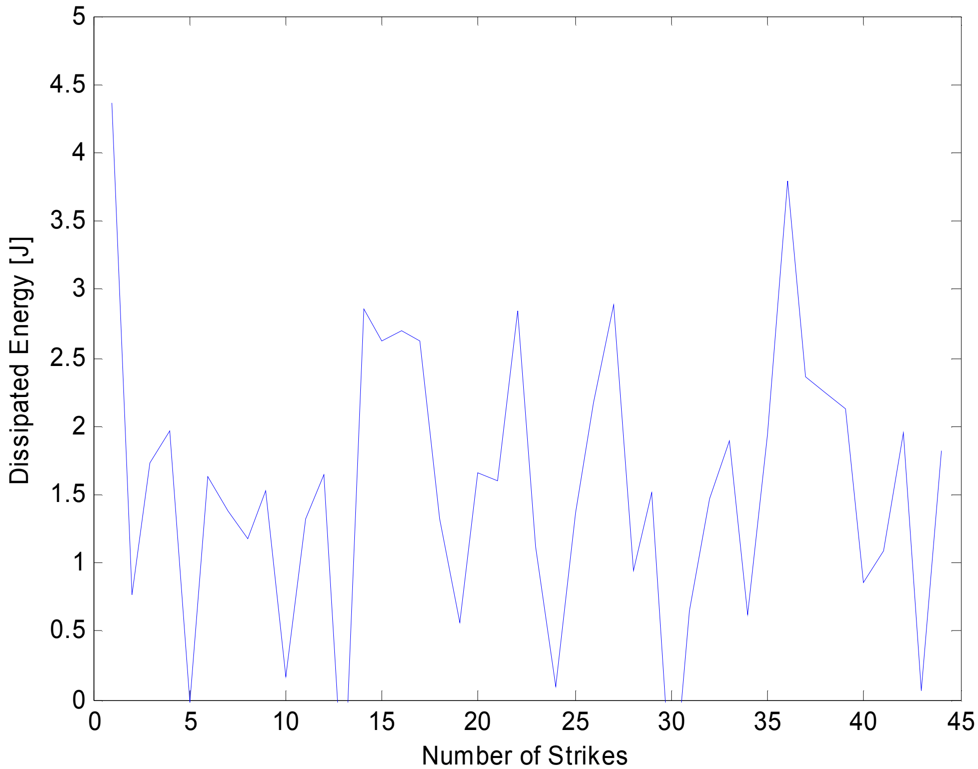

Figure A.18. Dissipated energy plot for specimen 20.

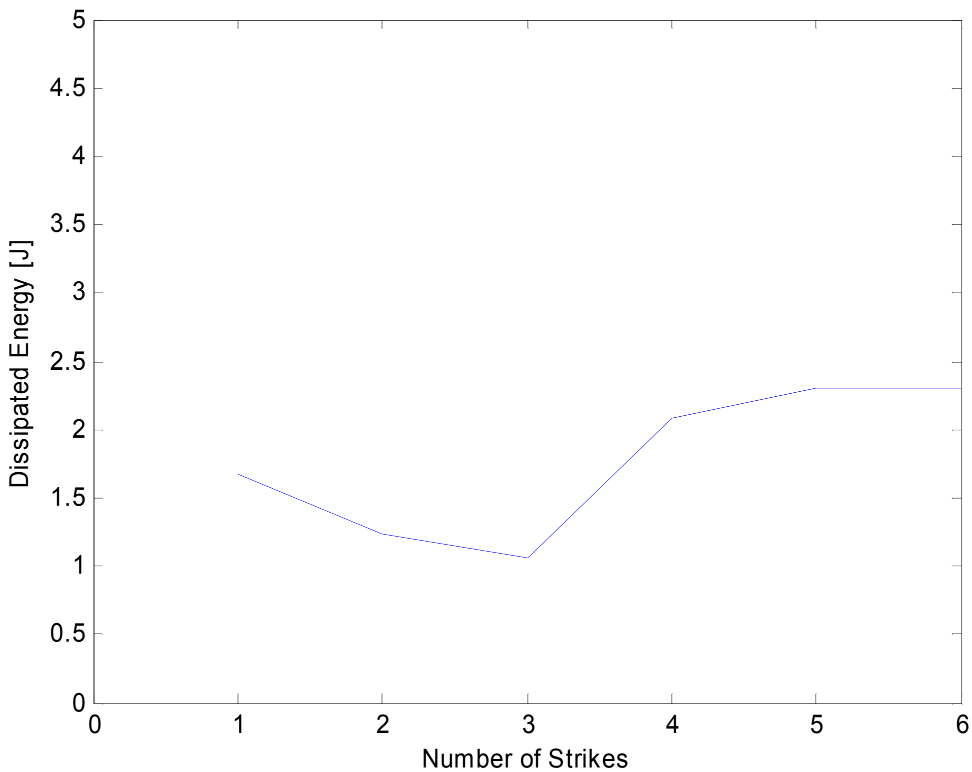

Figure A.19. Dissipated energy plot for specimen 21.

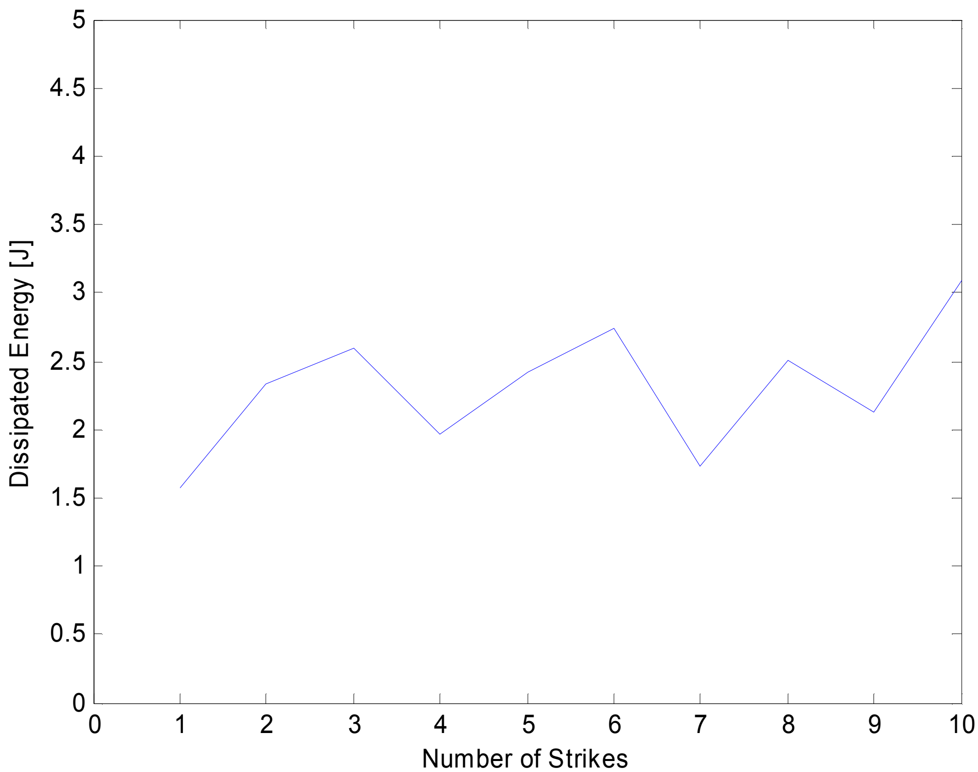

Figure A.20. Dissipated energy plot for specimen 22.

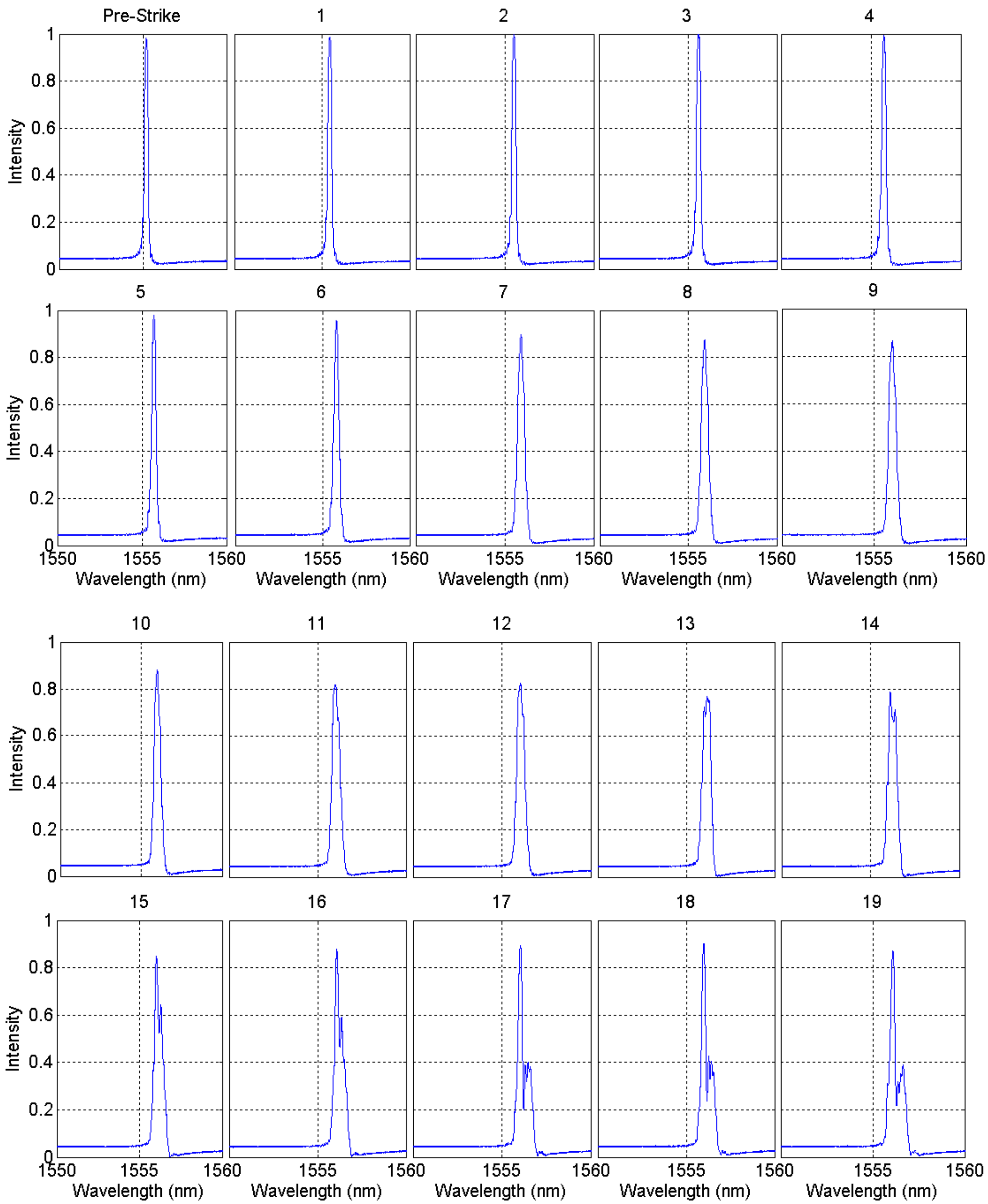

Figure A.21. Spectral response of specimen 24 through strike 19.

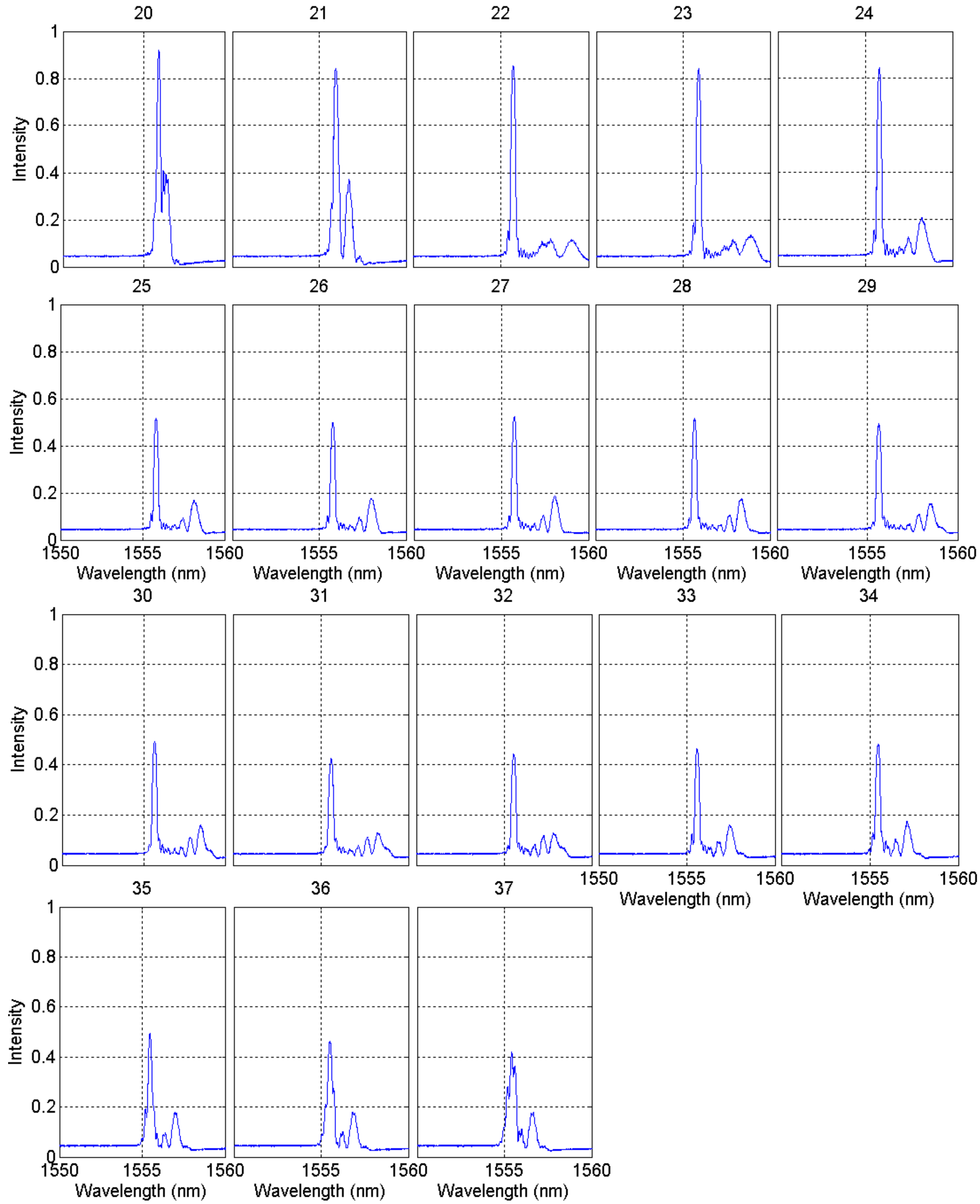

Figure A.22. Spectral response of specimen 24 from strike 20 through failure.

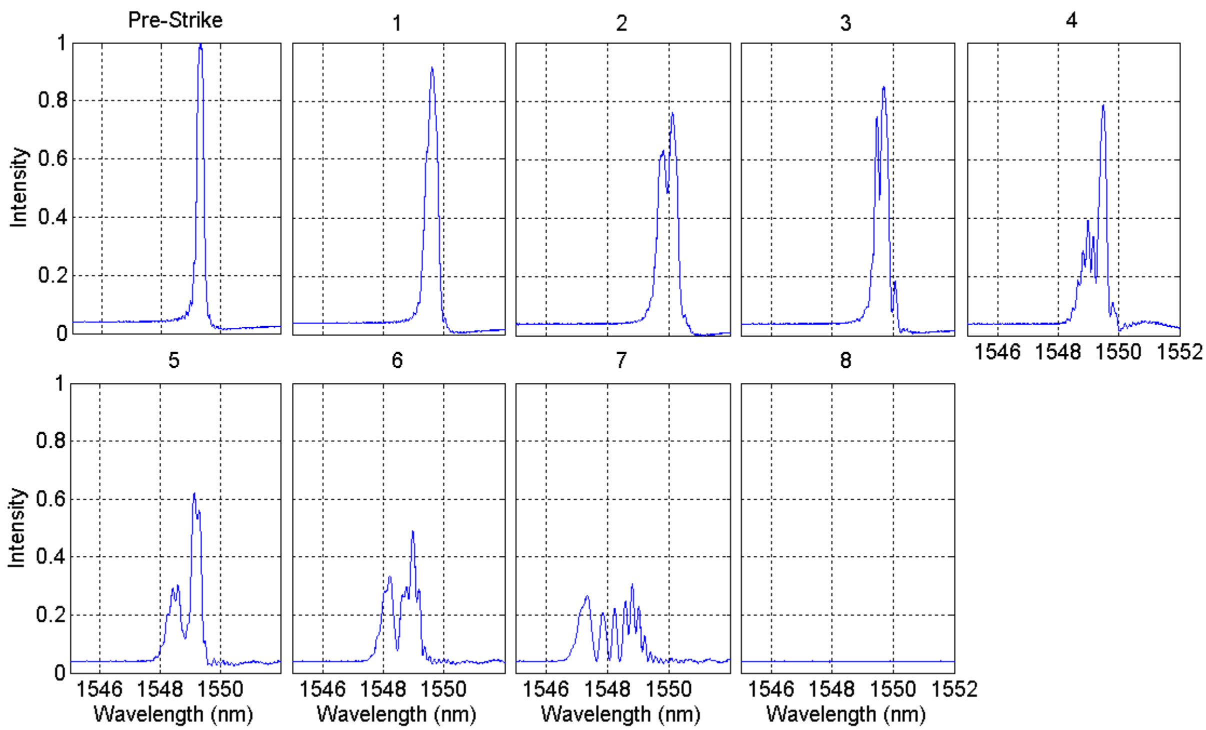

Figure A.23. Spectral response of specimen 25.

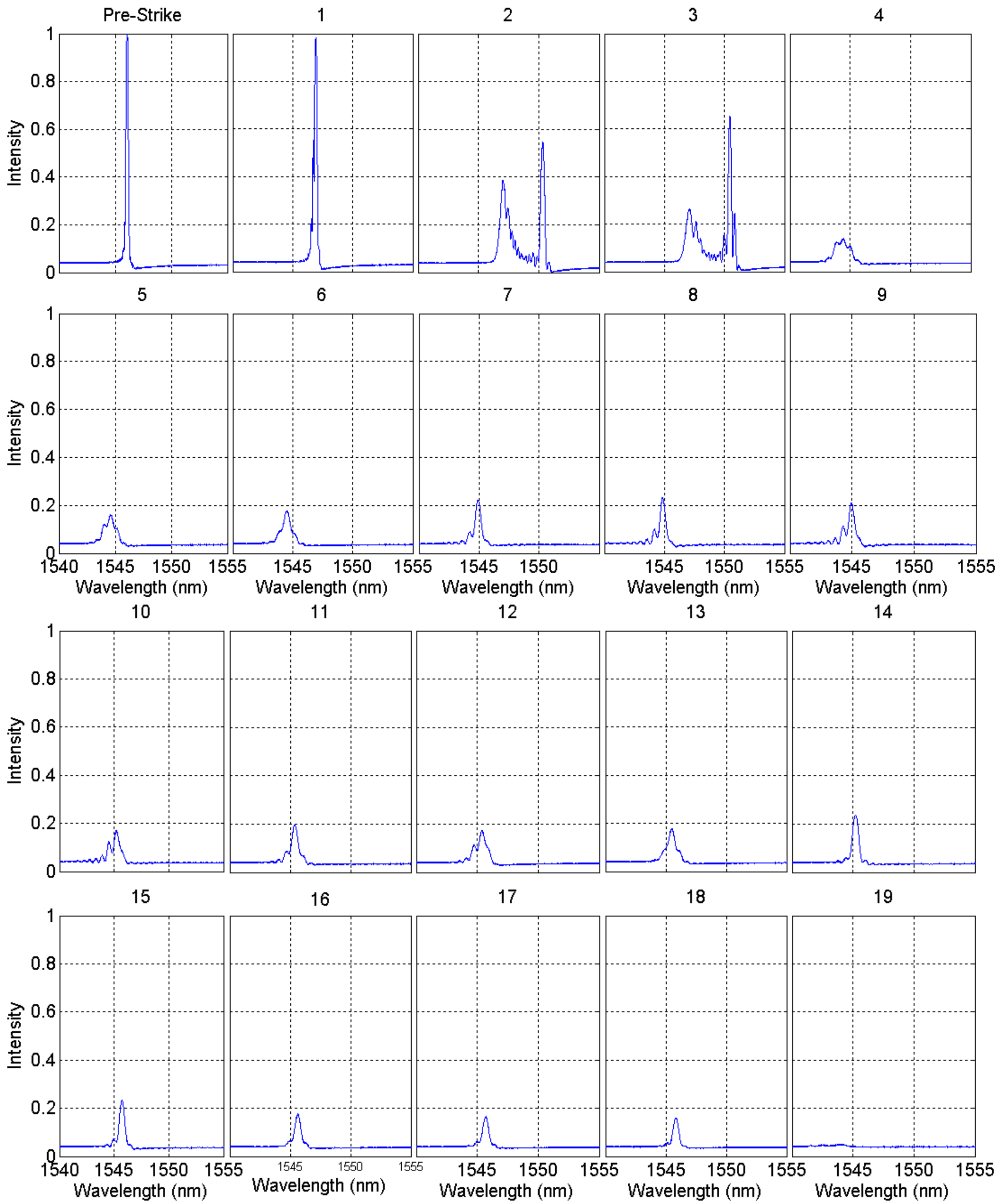

Figure A.24. Spectral response of specimen 26.